NRL Memorandum Report 5769

Current Enhancement for Hose-Unstable Electron Beams

R. F. FERNSLER, R. F. HUBBARD, B. HUI,
G. JOYCE, M. LAMPE AND Y. Y. LAU

Plasma Theory Branch
Plasma Physics Division

April 24, 1986

This work was supported by the Defense Advanced Research Projects Agency under ARPA Order No. 4395, Amendment No. 54, and monitored by the Naval Surface Weapons Center under Contract No. N60921-85-WR-W0239.

NAVAL RESEARCH LABORATORY
Washington, D.C.

SECURITY CLASSIFICATION OF THIS PAGE

REPORT DOCUMENTATION PAGE

1a. REPORT SECURITY CLASSIFICATION UNCLASSIFIED	1b. RESTRICTIVE MARKINGS
2a. SECURITY CLASSIFICATION AUTHORITY	3. DISTRIBUTION / AVAILABILITY OF REPORT Approved for public release; distribution unlimited.
2b. DECLASSIFICATION / DOWNGRADING SCHEDULE	
4. PERFORMING ORGANIZATION REPORT NUMBER(S) NRL Memorandum Report 5769	5. MONITORING ORGANIZATION REPORT NUMBER(S)
6a. NAME OF PERFORMING ORGANIZATION Naval Research Laboratory 6b. OFFICE SYMBOL (If applicable) Code 4790	7a. NAME OF MONITORING ORGANIZATION Naval Surface Weapons Center
6c. ADDRESS (City, State, and ZIP Code) Washington, DC 20375-5000	7b. ADDRESS (City, State, and ZIP Code) Silver Spring, MD 20910
8a. NAME OF FUNDING / SPONSORING ORGANIZATION DARPA 8b. OFFICE SYMBOL (If applicable)	9. PROCUREMENT INSTRUMENT IDENTIFICATION NUMBER
8c. ADDRESS (City, State, and ZIP Code) Arlington, VA 22209	10. SOURCE OF FUNDING NUMBERS PROGRAM ELEMENT NO. 62707E; PROJECT NO.; TASK NO.; WORK UNIT ACCESSION NO. DN680-415

11. TITLE (Include Security Classification)
Current Enhancement for Hose-Unstable Electron Beams

12. PERSONAL AUTHOR(S)
Fernsler, R. F., Hubbard, R. F., Hui, B., Joyce, G., Lampe, M. and Lau, Y. Y.

13a. TYPE OF REPORT	13b. TIME COVERED	14. DATE OF REPORT (Year, Month, Day)	15. PAGE COUNT
Interim	FROM _____ TO _____	1986 April 24	71

16. SUPPLEMENTARY NOTATION This work was supported by the Defense Advanced Research Projects Agency under ARPA Order No. 4395, Amendment No. 54, and monitored by the Naval Surface Weapons Center under Contract No. N60921-85-WR-W0239.

17. COSATI CODES		
FIELD	GROUP	SUB-GROUP

18. SUBJECT TERMS (Continue on reverse if necessary and identify by block number)
Electron beams; Charged particle beam; Circuit analysis; Current enhancement; Nonlinear hose instability; Resistive instabilities

19. ABSTRACT (Continue on reverse if necessary and identify by block number)

An electron beam injected into a conducting medium produces inductive electric fields. These fields drive conduction currents which, for stable beams, oppose the beam current and thereby reduce the total (net) current. For unstable beams which undergo large transverse displacements, the inductive fields can reverse direction and drive conduction current parallel to the beam current. An analytic and numerical treatment of the latter effect is presented to explain current enhancement as observed for electron beams propagating in gases at pressures above 10 torr. Keywords:

20. DISTRIBUTION / AVAILABILITY OF ABSTRACT	21. ABSTRACT SECURITY CLASSIFICATION
☒ UNCLASSIFIED/UNLIMITED ☐ SAME AS RPT. ☐ DTIC USERS	UNCLASSIFIED
22a. NAME OF RESPONSIBLE INDIVIDUAL R. F. Fernsler	22b. TELEPHONE (Include Area Code) (202) 767-6786
	22c. OFFICE SYMBOL Code 4790

DD FORM 1473, 84 MAR 83 APR edition may be used until exhausted. All other editions are obsolete.

SECURITY CLASSIFICATION OF THIS PAGE

CONTENTS

1. INTRODUCTION 1

2. CIRCUIT ANALYSIS 4

   2.1 Enhancement Due to Beam Expansion 9
   2.2 Enhancement Due to Beam Displacement 12
   2.3 Beams Propagating in Unbounded Neutral Gas 16

3. BEAM DISPLACEMENT IN A UNIFORM PLASMA 21

   3.1 Formulation and Solution 22
   3.2 Interpretation and Generalizations 25

4. COMPUTATIONAL MODELS 32

   4.1 SARLAC Particle Simulations 34
   4.2 Simplified SARLAC Simulations 36

5. CONCLUSION 38

ACKNOWLEDGMENTS 39

APPENDIX A: Inductance Formulae 40

APPENDIX B: Solution to Equation (46) 44

APPENDIX C: Extension to Two Dimensions 48

REFERENCES 70

CURRENT ENHANCEMENT FOR HOSE-UNSTABLE ELECTRON BEAMS

1. Introduction

The propagation of an energetic charged particle beam is controlled by the electromagnetic fields and forces which act on the beam. These fields and forces are modified by the electrical properties of the medium surrounding the beam. An assessment of these modifications is required to accurately predict beam advance. The net current, defined as the sum of the axial beam current and the axial conduction current induced in the medium, is a useful indicator of such modifications.

Beams passing through a gas ionize the gas and thereby change its conduction properties. In low-pressure gases a two-stream instability can arise which propels plasma electrons forward.[1] The forward-moving plasma electrons raise the net current for negatively charged beams but lower it for positively charged beams. For relativistic electron beams, net currents as large as three times the beam current have been observed.[1-3] These enhancements are accompanied by microwave emission characteristic of the plasma-electron oscillation frequency.

At higher pressures, binary collisions between the plasma electrons and the gas ions and molecules damp the two-stream instability and its associated current enhancement. Axial plasma currents then develop primarily from inductive effects which typically drive plasma return current opposite to the beam so as to minimize changes in magnetic flux. Net currents at high gas pressures are thus anticipated to be less than the beam current.[1]

Manuscript approved February 7, 1986.

Recent experiments performed on the Experimental Test Accelerator (ETA)[3-5] and elsewhere[6,7] have shown, however, that the net current can exceed the beam current, by as much as a factor of two, even at gas pressures of a few hundred torr. The absence of microwave emission at gas pressures above 10 torr indicates that this enhancement is not due to the two-stream instability. A second proposed explanation is energetic secondary electrons (delta rays) swept forward by the beam self-magnetic field. Estimates of delta-ray currents show that they are too small (less than 20 percent of the beam current) to account fully for the enhancement measured.[8]

In this paper we describe in detail a new and quantitative explanation[9,10] based on the observation that current enhancement at high gas pressures is associated with large transverse excursions of the beam.[3-6] The resistive hose instability which drives these excursions is particularly troublesome at gas pressures above a few torr, and develops from magnetic interactions between the beam current and plasma eddy currents that are inductively generated by transverse beam motion. Hosing of the beam spatially redistributes the net current density and thereby alters the effective system inductance. A rapid drop in the inductance causes the monopole electric field (in an azimuthal Fourier expansion) to reverse direction and drive plasma current parallel to the beam current. Dipole and higher-order fields complicate the redistribution of the current density but contribute little to the spatially integrated net current.

According to the present model, current enhancement is thus a natural outgrowth of large-amplitude hose instability. The inductive effects which produce the instability also produce current enhancement. The enhancement is, however, a nonlinear effect which is significant only for large beam displacements and cannot be seen with linearized codes and models[11-14] that are valid only during the onset and initial growth of the hose instability.

In this paper we present analytic and numerical treatments of inductive current enhancement. The circuit model in Sec. 2 provides a simple yet sound physical basis for current enhancement due either to beam expansion or beam displacement. In Sec. 3 we give a complete analytic field solution for beam displacement in a uniform conductivity channel. Here we show that current gains of three or more are possible if the beam actually strikes a metallic wall. Consideration of beam dynamics and conductivity evolution suggests, however, that the hose instability is unlikely to produce current gains much above a factor of two. In Sec. 4 we present self-consistent numerical simulations of beam propagation using a new nonlinear particle code, SARLAC, which treats both large-amplitude hose instability and current enhancement. Substantial enhancement (~ 70 percent) is seen for beam displacements out to half the wall radius, in agreement with the ETA experiments. Because cause-and-effect relationships between current enhancement and various beam and cavity parameters are obscured by the complexity and sensitivity of the hose instability, we also present simplified simulations using a prescribed dynamical beam displacement to further elucidate and verify the analytic models.

2. Circuit Analysis

We seek in this section to provide a simple physical basis for current enhancement due either to beam displacement or expansion. A few models suffice to demonstrate the effect.

A circuit model is often used to compute the net current I_n as a function of beam current I_b. For stable beams of constant radius, the circuit model reduces at high gas pressure to[1]

$$L \frac{\partial}{\partial t} I_n = - (I_n - I_b)R \qquad (1)$$

where L is the circuit inductance, R is the plasma resistance, and $(I_n - I_b)$ is the plasma current. This equation relates changes in the magnetic flux LI_n to diffusion of magnetic field through the plasma resistance R. An important consequence of this equation is that the maximum I_n is less than the maximum I_b (provided $I_n \leq I_b$ initially). Equation (1) therefore precludes current enhancement:

$$F = I_n^{(max)}/I_b^{(max)} \leq 1.$$

Equation (1) is valid, however, only if the inductance L is constant. In general, the inductance is not constant but is a geometrical parameter which depends on the spatial distribution of the beam, plasma, and boundary currents. The boundary current is presumed to reside in a metallic pipe which encompasses the beam and plasma. Beam displacement and expansion alter the current distribution and thereby alter the inductance L and flux LI_n. To include these effects an additional term proportional to $I_n \frac{\partial L}{\partial t}$ must be added to the left-hand side of Eq. (1). This additional term is what produces current enhancement. Such a possibility has been previously recognized but not quantified.[5,15]

We consider first the case where the plasma conductivity is sufficiently high to suppress electrostatic effects everywhere inside a perfectly conducting (metallic) pipe at radius b. In addition we make the long-wavelength and low-frequency approximations:

$$b \frac{\partial}{\partial z}, \frac{b}{c} \frac{\partial}{\partial t} << 1 \tag{2}$$

where c is the speed of light. Maxwell's equations then reduce to the magnetostatic Faraday-Ampere law for the axial vector potential A_z:

$$\nabla_\perp^2 A_z = - \frac{4\pi}{c} (J_b + \sigma E_z), \tag{3}$$

with the axial electric field given by

$$E_z = - \frac{1}{c} \frac{\partial A_z}{\partial t}. \tag{4}$$

The plasma conductivity σ and beam current density J_b are specified functions of $(\underline{r}_\perp, t)$. The boundary condition is

$$A_z = 0 \tag{5}$$

at $r = b$. In subsection 2.3 we extend the analysis to include electrostatic effects which arise if the medium is poorly conducting or non-conducting at radii that are large but still within the pipe. A complete numerical treatment is given in Sec. 4.

Equations (3)-(5) may be reduced to a simple circuit equation provided the plasma conductivity is azimuthally symmetric about the pipe center. To show this, consider the azimuthally averaged (monopole) component of the electric field:

$$E_{zo}(r,t) = \frac{1}{2\pi}\int_0^{2\pi} d\theta\, E_z. \tag{6}$$

By suitably integrating Eq. (3) and applying Eq. (4) and boundary condition (5), one finds that

$$E_{zo} = -\frac{2}{c^2}\int_r^b \frac{dr}{r}\frac{\partial I}{\partial t} \tag{7}$$

where I is the net current flowing within radius r:

$$I(r,t) = \int_0^r dr\, r \int_0^{2\pi} d\theta\, (J_b + \sigma E_z). \tag{8}$$

The plasma current equals the difference between the net current and the beam current:

$$I_n - I_b = \int_0^b dr\, r \int_0^{2\pi} d\theta\, \sigma E_z. \tag{9}$$

For azimuthally symmetric conductivity, only the monopole field contributes. Hence,

$$I_n - I_b = \int_0^b dr\, 2\pi r\sigma\, E_{zo} = -\frac{2}{c^2}\int_0^b dr\, 2\pi r\sigma \int_r^b \frac{dr'}{r'}\frac{\partial I}{\partial t}. \tag{10}$$

This equation or its equivalent applies to all the analytic work presented herein but not to the numerical simulations in Sec. 4 which allow the conductivity to be azimuthally asymmetric.

To express Eq. (10) in a form similar to Eq. (1), we define the radial profiles of the net current and plasma conductance, respectively, by

$$\hat{I}(r,t) = I(r,t)/I_n(t) \tag{11}$$

and

$$\hat{\Sigma}(r,t) = R \int_o^r dr\ 2\pi r\sigma \tag{12}$$

where

$$R(t) = \left(\int_o^b dr\ 2\pi r\sigma\right)^{-1} \tag{13}$$

is the plasma resistance per unit length. Equation (10) may then be rewritten as

$$L \frac{\partial}{\partial t} I_n + \dot{L} I_n = - (I_n - I_b)R \tag{14}$$

where we define $L(t)$ and $\dot{L}(t)$ as

$$L(t) = \frac{2R}{c^2} \int_o^b dr\ 2\pi r\sigma \int_r^b \frac{dr'}{r'} \hat{I}$$

and

$$\dot{L}(t) = \frac{2R}{c^2} \int_o^b dr\ 2\pi r\sigma \int_r^b \frac{dr'}{r'} \frac{\partial \hat{I}}{\partial t}.$$

Integration by parts and use of definition (12) produces an effective system inductance given by

$$L(t) = \frac{2}{c^2}\int_o^b \frac{dr}{r}\,\hat{\Sigma}\,\hat{I} \tag{15}$$

and a parameter $\dot{L}$ given by

$$\dot{L}(t) = \frac{2}{c^2}\int_o^b \frac{dr}{r}\,\hat{\Sigma}\,\frac{\partial \hat{I}}{\partial t}. \tag{16}$$

Circuit equation (14) together with definitions (13), (15), and (16) is an equivalent and exact representation of the Faraday-Ampere laws (3)-(5), provided that the plasma conductivity is azimuthally symmetric about the pipe center. Even for asymmetric conductivity, Eq. (14) is often a good approximation. In this equation, the effective system inductance L is a geometrical parameter determined by the location of the pipe boundary and by the spatial distributions of the plasma conductivity and net current. The parameter $\dot{L}$, which was absent from the original circuit equation (1), represents a change in inductance due to redistribution of the net current. Note however that $\dot{L}$ does not equal $\frac{\partial L}{\partial t}$ unless the distribution of plasma conductivity is constant ($\frac{\partial}{\partial t}\hat{\Sigma} = 0$). Current enhancement is possible only if $\dot{L} < 0$.

The circuit model offers a simple yet potentially accurate means for computing the net current. The accuracy is limited primarily by our ability to determine R, L, and $\dot{L}$ which depend (weakly) on the spatial distribution of the plasma current and conductivity. In this paper we make only partial use of the circuit equation. We nonetheless provide in Appendix A some inductance formulae which demonstrate the dependence of L on geometry. When using these

formulae to compute the net current for a prescribed beam perturbation, the parameter $\dot{L}$ should generally be assigned a value from one-half to one times $\frac{\partial L}{\partial t}$.

2.1 Enhancement Due to Beam Expansion

To demonstrate the utility of the circuit model, consider current enhancement arising from self-similar expansion of an on-axis beam and plasma. This example is chosen for illustrative purposes only. We later conclude, from consideration of beam dynamics, that beam expansion due to axisymmetric instabilities such as sausage and hollowing is unlikely to produce current gains above unity. The high current gains observed experimentally are shown in subsection 2.2 and following to arise from hose-induced beam displacement with expansion as a secondary effect.

For self-similar expansion, the distribution functions for current and conductance become equal:

$$\hat{\Sigma}(r,t) = \hat{I}(r,t). \tag{17}$$

Equations (15) and (16) then yield

$$\dot{L} = \frac{1}{2} \frac{\partial L}{\partial t} \tag{18}$$

so that circuit equation (14) reduces to

$$L \frac{\partial I_n}{\partial t} + \frac{1}{2} I_n \frac{\partial L}{\partial t} = - (I_n - I_b)R. \tag{19}$$

An alternative form is the energy conservation relationship

$$\frac{\partial}{\partial t}\left(\frac{1}{2} L I_n^2\right) = -\left[(I_n - I_b)R\right] I_n \tag{20}$$

where $\frac{1}{2} L I_n^2$ is the stored magnetic field energy and $[(I_n - I_b)R] I_n$ is the rate at which the current I_n extracts energy ohmically from the inductive electric field $(I_n - I_b)R$.

Rapid expansion maximizes current enhancement and reduces Eq. (20) to conservation of magnetic field energy:

$$\delta(L I_n^2) \to 0. \tag{21}$$

Inserting inductance formula (A1) of Appendix A into this relationship yields a maximum current gain for an expanding on-axis beam and plasma given by

$$F = I_n/I_b$$

$$= F_o \left[\frac{\ell n(b/a_o) + \alpha}{\ell n(b/a) + \alpha}\right]^{1/2}. \tag{22}$$

Here a_o is the initial beam radius, a is the expanded beam radius, $F_o = I_{no}/I_b \leq 1$ is the current gain immediately prior to expansion, and $\alpha^2 \leq \frac{1}{4}$ is a geometrical constant. Examination of Eq. (19) reveals, however, that result (22) is valid only if the beam and plasma expand in a time short compared with the monopole decay time,

$$\tau_o = L/R. \tag{23}$$

Otherwise, ohmic heating extracts sufficient energy during the expansion that relationship (21) is a poor approximation.

For the ETA experiments where $b/a_o = 10$, Eq. (22) predicts that current enhancements of 30 percent ($F = 1.3$) are possible if $F_o = 1$ and if the beam radius doubles ($a/a_o > 2$) in less than a monopole decay time τ_o. The simulation results presented in Sec. 4.1 show such expansion.

Several observations should be made regarding current enhancement due to beam expansion. The first is that axisymmetric instabilities such as the sausage and hollowing modes[16-18] can cause the beam to expand and inductively raise the net current. Yet such expansion is unlikely to produce current gains above unity. The reason is that beam expansion due to the axisymmetric resistive instabilities occurs because on-axis plasma current initially flows opposite to the beam current and magnetically repels it; as a result, $F_o \leq 1/2$ at the onset of the axisymmetric instabilities.[16,18] Although beam expansion increases F, this in turn strengthens the magnetic pinch force on the beam which restrains or reverses further expansion. Usually[18] a dynamic balance is reached, or further radial oscillations occur, but with $F < 1$.

A second observation, direct from result (22), is that the pipe radius b is the radial scale length governing current enhancement. This is because the inductance L changes appreciably only when the beam radius (or beam displacement, as shown in Sec. 2.2) is non-negligible compared with b. One might surmise that current enhancement cannot occur if the pipe is absent or very large. This conclusion is incorrect, however, as shown in Sec. 2.3 where we incorporate electrostatic effects into the circuit analysis. There we show that b is really the monopole boundary radius at which the azimuthally averaged field E_{zo} falls to zero, and that b is finite if the medium becomes non-conducting at large radii ($r\sigma \to 0$ as $r \to \infty$).

A third point is that beam expansion is a secondary effect of the resistive hose instability: as the beam displaces far off axis, it separates from the centroid of the net current so that the pinch force on the beam weakens and the beam expands. The circumstances of this expansion are sufficiently complex that Eq. (22) should be treated as but a rough guide for current enhancement due to beam expansion, as distinct from enhancement due to beam displacement alone.

A fourth observation is that the energy source responsible for producing and driving the plasma currents is not kinetic beam energy directly but magnetic field energy. In the case of beam expansion the stored magnetic field energy not only drives the plasma currents but also accelerates the beam to higher energy.

2.2 Enhancement Due to Beam Displacement

Consider now current enhancement resulting from transverse displacement of a rigid-rod beam of fixed radius a. We again assume that the plasma conductivity is azimuthally symmetric about the pipe center. Only the monopole electric field then contributes to the net current. For other conductivity configurations the dipole and higher-order fields contribute as well.

A simple model which provides a semi-quantitative estimate of current enhancement is as follows. Imagine a beam which originally resides in a fixed plasma channel centered within a pipe of radius b. The plasma channel and beam have a small radius $a \ll b$.

A sudden displacement of the beam to an off-axis location r_b perturbs the plasma currents and wall currents. The values of these currents immediately after the displacement can be readily computed provided: (i) the displacement

occurs instantaneously; and (ii) the displaced beam is wholly outside the plasma but wholly inside the pipe, i.e.,

$$2a < r_b < b - a. \tag{24}$$

The plasma then behaves as a perfect conductor while the beam can be treated as a line current at r_b.

A circuit treatment of this problem is given in Appendix A. Here we give for comparison a field treatment. We begin by dividing the plasma current into two components. The homogeneous component is derived by imagining that the beam current I_b is suddenly moved from inside the plasma to outside the pipe. Because magnetic flux remains trapped within the plasma, the homogeneous plasma current is given by

$$I_{ph} = I_{no} \tag{25}$$

where I_{no} is the net current just prior to beam displacement.

The driven component of the plasma current is derived by imagining that the line current I_b is suddenly moved from outside the pipe to the location r_b inside. For this problem the vector potential A_z is zero both at the pipe boundary, $r = b$, and everywhere within the plasma, $r \leq a$. These two boundary conditions determine the driven (surface) plasma current I_{pd}.

We evaluate I_{pd} by integrating the Faraday-Ampere law (3) over r and θ to obtain for $r > a$:

$$\frac{dA_{zo}}{dr} = -\frac{2}{c^2 r}\left[I_{pd} + I_b\, H(r - r_b)\right] \tag{26}$$

where H is the Heaviside step function and where the monopole vector potential is defined by

$$A_{zo}(r) = \frac{1}{2\pi} \int_0^{2\pi} d\theta \; A_z(r,\theta). \tag{27}$$

Integrating Eq. (26) and applying the boundary condition

$$A_{zo}(a) = 0 \tag{28}$$

yields

$$A_{zo}(r) = - \frac{2}{c^2} [I_{pd} \ln(r/a) + I_b H(r - r_b) \ln(r/r_b)]. \tag{29}$$

Applying the boundary condition

$$A_{zo}(b) = 0 \tag{30}$$

produces

$$\frac{I_{pd}}{I_b} = - \frac{\ln(b/r_b)}{\ln(b/a)}. \tag{31}$$

Solution (31) for the driven plasma current I_{pd} has a simple physical basis. Injecting a current source I_b between two conducting surfaces drives return current in each of the surfaces. The total return current equals $-I_b$. The fraction of return current flowing in either one of the surfaces is a function of the surface geometry and of the source location. For coaxial conductors of inner and outer radii a and b, the fraction flowing on the inner (plasma) conductor is given by Eq. (31).

The overall net current inside radius b is the sum of the beam current I_b and the plasma currents I_{ph} and I_{pd}. From Eqs. (25) and (31) we thus have

$$F = \frac{I_b + I_{ph} + I_{pd}}{I_b}$$

$$= F_o + \frac{\ln(r_b/a)}{\ln(b/a)} \qquad (32)$$

where $F_o = I_{no}/I_b$ is the current gain immediately prior to pushing the source off axis. Typically $F_o < 1$ due to plasma return currents which were induced when the on-axis source was originally injected into the plasma.

Result (32) for the current gain F was derived assuming instantaneous beam displacement. We show in Appendix A, however, that magnetic flux relaxes slowly on a monopole decay time, $\tau_o = L/R$. Result (32) can thus still be applied provided the beam moves off axis to r_b in a finite but short time

$$\tau(r_b) < \tau_o = \frac{2}{Rc^2}[\ln(b/a) + \alpha]. \qquad (33)$$

Although the net current and monopole fields relax slowly, the dipole and higher-order fields (in an azimuthal Fourier decomposition) relax rapidly on a dipole decay time given by[11]

$$\tau_d = (2Rc^2)^{-1}. \qquad (34)$$

Comparison of Eqs. (33) and (34) reveals that the monopole and dipole decay times are typically related by

$$\tau_o/\tau_d = 4[\ln(b/a) + \alpha] >> 1. \qquad (35)$$

The plasma current thus spatially redistributes before it decays.

The distinction between decay and redistribution of the plasma eddy currents is important in understanding hose-induced current enhancement. The resistive hose instability develops from a phase lag between dynamical beam displacement and redistribution of the dipole fields. In the absence of a phase lag, the dipole fields produce a restoring force which causes oscillation but no growth in beam displacement.[14] The dipole decay time τ_d controls the phase lag and thus characterizes the growth rate of the instability. During a monopole time $\tau_o >> \tau_d$, large-amplitude hose displacement is possible. A hose-unstable beam of long duration ($>> \tau_d$) is thus likely to produce, given sufficient propagation distance, a significant increase in the net current.

For the ETA experiments where $b/a = 10$, Eq. (32) predicts that current enhancements of 30 percent ($F = 1.3$) are possible even for modest displacements of a few beam radii, $r_b = 2a$. A current enhancement of nearly 100 percent ($F \to 2$) is possible for large displacements, $r_b \to b - a$.

2.3 Beams Propagating in Unbounded Neutral Gas

In the preceding treatments we assumed that a metallic drift tube was present and that the gas conductivity everywhere within the drift tube was sufficiently large to ensure space-charge neutralization. If this is not the case, electrostatic terms must be included in the field and circuit equations. We show here, using a revised circuit analysis, that the phenomenon of hose-induced current enhancement is qualitatively unchanged even if the drift tube is absent or lies far outside the region where space-charge neutralization occurs. The principal revision is that the monopole boundary radius b, where $E_{zo} = 0$, is not the pipe radius but a "vacuum radius" beyond which the space-charge fields are unsuppressed.

The revised circuit analysis is based on Maxwell's equation for the axial electric field:

$$\nabla_\perp^2 E_z + \frac{\partial^2 E_z}{\partial z^2} - \frac{1}{c^2}\frac{\partial^2 E_z}{\partial t^2} = \frac{4\pi}{c^2}\frac{\partial}{\partial t}(J_b + \sigma E_z) + 4\pi\frac{\partial \rho}{\partial z} \tag{36}$$

where ρ is the charge density. As shown by E. P. Lee,[22] this equation can be simplified for beams which are both ultrarelativistic,

$$\beta \equiv v_z/c \to 1, \tag{37}$$

and paraxial,

$$\frac{a}{\beta c}\frac{d}{dt} = a\left(\frac{\partial}{\partial z}\right)_\tau = O(a/\lambda_\beta) \ll 1. \tag{38}$$

Here v_z is the beam axial velocity, a is a characteristic beam radius, $\tau \equiv t - z/\beta c$ is a temporal variable designating a particular beam slice, and $\lambda_\beta \equiv 2\pi a(\beta\gamma mc^3/eI_n)^{1/2}$ is a characteristic betatron wavelength. The electron charge-to-mass ratio is e/m, and $\gamma \equiv (1-\beta^2)^{-1/2}$ is the usual relativistic factor.

By changing variables from (z,t) to (z,τ) and by setting $\beta = 1$ and $\left(\frac{\partial}{\partial z}\right)_\tau = 0$, we can rewrite Eq. (36) as

$$\nabla_\perp^2 E_z = \frac{4\pi}{c^2}\frac{\partial}{\partial \tau}(J_b + \sigma E_z - \rho c) \tag{39}$$

which is typically valid to order $\gamma^{-2} \ll 1$ and $a/\lambda_\beta \ll 1$. The neglect of axial derivatives is denoted the "frozen-field approximation" and follows from the paraxial condition (38). The full Lee field equations, which are presented in Sec. 4, employ an additional approximation not needed here.

For azimuthally symmetric conductivity, we may duplicate the procedure in Sec. 2 and reduce Eq. (39) to a circuit equation for the net conduction current I_n:

$$L \frac{\partial}{\partial \tau} I_n + \dot{L} I_n = - (I_n - I_b) R \tag{40}$$

where the effective system inductance is now defined by

$$L(\tau) = \frac{2}{c^2} \int_0^\infty \frac{dr}{r} \hat{\Sigma} (\hat{I} - \hat{Q}) \tag{41}$$

and the parameter $\dot{L}$ is defined by

$$\dot{L}(\tau) = \frac{2}{c^2} \int_0^\infty \frac{dr}{r} \hat{\Sigma} \frac{\partial}{\partial \tau} (\hat{I} - \hat{Q}). \tag{42}$$

Here the radial profile of the distributed charge is given by

$$\hat{Q}(r,\tau) = Q_n^{-1} \int_0^r dr\, r \int_0^{2\pi} d\theta\, \rho \tag{43}$$

while the distributed net charge is given from charge conservation by

$$Q_n(\tau) = \int_0^\infty dr\, r \int_0^{2\pi} d\theta\, \rho = I_n(\tau)/c. \tag{44}$$

The revised circuit equations (40)-(42) closely resemble the earlier versions (14)-(16). The difference is the presence of $\hat{Q}$ and the <u>apparent</u> absence of a finite cutoff radius b in the inductance formulae. Recall that a finite cutoff is required for current enhancement to occur.

A finite cutoff in fact exists. At some large radius b outside the beam, the conductivity becomes so low that the medium acts as a vacuum: typically,

$$4\pi\sigma r/c \lesssim 0.1 \qquad (45)$$

for all $r \geq b$. Beyond the vacuum radius b, the profile functions $\hat{I}$ and $\hat{Q}$ equal unity by definition. Inductance formulae (41) and (42) can thus be terminated without approximation at $r = b$.

For intense tightly pinched beams, conductivity in the corona region outside the beam is generated both from collisional ionization by the expanded beam head and from avalanche ionization in the radial electrostatic field. For such beams, the vacuum radius b is typically large (>> a) and insensitive to displacement or expansion of the beam body. Moreover, the corona conductivity rises rapidly inside b so that space charge accumulates near $r = b$. Behind the beam head, the charge density ρ and profile $\hat{Q}$ therefore approach zero for $r < b$, and Eqs. (40)-(42) become virtually indistinguishable from Eqs. (14)-(16). Current enhancement for a given perturbation of the beam body, where large hose growth is most probable, is thus almost the same whether or not a metallic boundary is present at $r = b$ (or at $r > b$).

The presence or absence of a metallic wall beyond the vacuum radius does not directly affect current enhancement because a vacuum boundary, like a metallic boundary, shorts out the monopole electric field E_{zo} which determines the net current for axisymmetric conductivity. Even for asymmetric conductivity, the monopole contribution usually dominates because: (i) σ is positive definite and thus has a large monopole component; and (ii) the dipole and higher-order azimuthal components of E_z decay much more rapidly than E_{zo}. Circuit equations (40)-(42) are thus usually a fair approximation to Eq. (39) even if σ is asymmetric.

The nature of the boundary can, of course, strongly affect the dipole and higher-order fields which control beam displacement. Large displacements are restrained, for example, by metallic boundaries which carry a return current that magnetically repels the beam, but are not restrained by vacuum boundaries where the return current and associated wall forces are absent or weak. The nature of the boundary can thus alter the degree of hose growth and consequent current enhancement, but does not alter the occurrence or qualitative behavior of the phenomenon.

3. Beam Displacement in a Uniform Plasma

In this section we consider a broad channel with uniform conductivity extending out to the metallic boundary. The extension in σ has a pronounced effect on current enhancement and represents the opposite limit to the narrow conductivity channels considered in Sec. 2.2. Unfortunately, a circuit analysis is impractical for extended σ because the spatial distribution of the plasma current can no longer be estimated a priori. We give instead a complete field solution for a problem which is analytically tractable: viz., an infinitesimally thin current source moving at constant transverse velocity u through a medium of uniform and constant conductivity σ. The underlined words represent the simplifying assumptions. In subsection 3.2 we discuss the consequences of relaxing some of these assumptions.

The solution to our model problem can be expressed in terms of two dimensionless parameters: $r_b(t)/b$ and δ_o/b where $r_b(t)$ is the beam displacement and $\delta_o \equiv c^2/4\pi\sigma u$ is identified as a skin depth. The solution would depend on a third parameter, a/b, if the source were of finite thickness.

Solutions are given with and without displacement currents included in the analysis. As expected, the displacement currents are unimportant provided $u/c \leq 0.1$. We show in Appendix C that the solutions are insensitive to the cavity shape as well.

We describe this problem and its solution in considerable detail because it provides additional insight and because it reveals two new features. The first is that current enhancement in broad conductivity channels does not become appreciable until the current source approaches to within a skin depth of the conducting boundary. The second and more surprising feature is that for $\delta_o/b \ll 1$, a current gain of three or more is attained as the source is

about to strike the boundary. Recall that Eq. (32) restricts the current gain for a narrow (and stationary) conductivity channel to a maximum value of two. Extending the plasma conductivity out to the boundary thus reduces the current gain for modest displacements, $r_b \leq b/2$, but increases the gain for large displacements $r_b \to b$.

3.1 Formulation and Solution

For simplicity we consider a one-dimensional system in slab geometry. [The extension to a two-dimensional system may be found in Appendix C.] In our model, an infinitesimally thin current sheet of surface density I_b flows in the z-direction. The current sheet is initially located midway between two perfectly conducting plates, P_L and P_R, at $x = 0$ and $x = \ell$, respectively. We assume that the medium between P_L and P_R is characterized by a constant electrical conductivity σ. We further assume that the current sheet has been situated at $x = x_b = \ell/2$ for a long time so that all plasma current has decayed to zero at $t = 0$. For $t \geq 0$, the current sheet is given a uniform x-ward motion, i.e., $x_b(t) = \ell/2 + ut$ where the speed u is assumed to be constant.

The fields are governed by the diffusion equation for the longitudinal vector potential A_z:

$$-\frac{c}{4\pi}\frac{\partial^2 A_z}{\partial x^2} = -\frac{\sigma}{c}\frac{\partial A_z}{\partial t} + I_b\delta(x-x_b(t)); \quad 0 < x < \ell, \quad 0 < t < \ell/2u. \tag{46}$$

Here δ is the Dirac delta function, and displacement currents are (initially) ignored. The boundary condition is

$$A_z(0,t) = A_z(\ell,t) = 0. \tag{47}$$

The initial condition is

$$A_z(x,0) = (\pi \ell I_b/c)\,(1 - |2x - \ell|/\ell), \tag{48}$$

reflecting the assumption that a steady magnetic field is established prior to $t = 0$.

The current enhancement factor is given by

$$F(t) = 1 - (\sigma/I_b c) \int_0^{\ell} dx\, \partial A_z/\partial t, \tag{49a}$$

where $-(\sigma/c)\partial A_z/\partial t$ is the current density induced within the conductivity channel. Alternatively,

$$F(t) = \frac{1}{I_b}\left[-\frac{c}{4\pi}\frac{\partial A_z}{\partial x}\bigg|_{x=\ell} + \frac{c}{4\pi}\frac{\partial A_z}{\partial x}\bigg|_{x=0}\right] \tag{49b}$$

where the square bracket represents the wall currents. Equation (49b) is readily obtained by integrating Eq. (46) from $x = 0$ to $x = \ell$.

The diffusion equation (46), together with its associated initial conditions and boundary conditions, is solved in Appendix B. There we show that just before the current sheet makes contact with P_R, the current enhancement factor is given by [cf. Eq. (B13)]

$$F = 1 + \tanh\left(\frac{\pi v}{2}\right) + \frac{4}{\pi}\sum_{\substack{n=1 \\ n\ \mathrm{odd}}}^{\infty} (-1)^{\frac{n-1}{2}}\, e^{-\frac{n^2\pi}{2v}}\, \frac{v^2}{n(n^2 + v^2)} \tag{50}$$

where

$$v = \tau_{dif}/\tau_t = 4u\sigma\ell/c^2 \tag{51}$$

is the ratio of the characteristic diffusion time $\tau_{dif} \equiv 2\sigma\ell^2/c^2$ to the transit time $\tau_t \equiv \ell/2u$. The infinite sum in Eq. (50) converges rapidly for finite values of v.

The enhancement factor F, as given by Eq. (50), is plotted in Fig. 1 as a function of the normalized velocity v. The most interesting and unexpected feature is that F approaches an asymptotic limit of three as v becomes large. From Fig. 1, one sees that $F > 2$ for $v \geq 1$. For $v \leq 0.5$, a good approximation is $F = 1 + \pi v/2$, as is readily verified from Eq. (50) and is also easily deduced from a quasi-static argument.

The time evolution of F gives additional insight into the physical processes. We show in Appendix B that

$$F(t) = 1 + \frac{4}{\pi} \sum_{\substack{n=1 \\ n\ \text{odd}}}^{\infty} \frac{(-1)^{\frac{n-1}{2}}}{n(n^2 + v^2)} \left\{-v^2 \cos\left(\frac{n\pi t}{2\tau_t}\right) + nv \sin\left(\frac{n\pi t}{2\tau_t}\right) + v^2 e^{-\frac{n^2 t}{v\tau_t}}\right\}. \tag{52}$$

This infinite series is absolutely and uniformly convergent for all $t \geq 0$. The evolution of F as a function of normalized time t/τ_t is shown in Fig. 2 for various values of v. Observe that current enhancement becomes appreciable only when x_b reaches within a "boundary layer" width of P_R, i.e., when $t - \tau_t \leq \tau_t/v$. The width of this boundary layer (skin depth) is on the order of ℓ/v, as suggested by Fig. 2. This may also be deduced by a dimensional argument from the diffusion Eq. (46).

In Appendix C we extend our model to two transverse dimensions and represent the beam as a current-carrying wire which moves at constant transverse velocity inside a waveguide filled with conducting medium. We find that all qualitative features of the one-dimensional model, including the

maximum enhancement factor of three, are essentially unchanged. Indeed, these features are of such a universal nature that they are independent of the initial location of the current source as long as $\tau_{dif} >> \tau_t$. In the next subsection we discuss the effects of finite beam thickness and of nonuniform velocity.

3.2 Interpretation and Generalizations

To elucidate the preceding unexpected features of a boundary-layer effect and $F \to 3$ for $v >> 1$, we decompose the induced plasma current into two parts. The first part is associated with relaxation of the magnetic field which was present prior to $t = 0$. This part is independent of the motion of the current source. The second part is due to the transverse motion of the current source, but is independent of the initial magnetic field. Such a decomposition also enables us to predict the qualitative behavior when the beam motion is nonuniform or the beam size is finite. These generalizations, together with the influence of the displacement currents, will be addressed later.

The above mentioned decomposition is equivalent to expressing the solution $A_z(x,t)$ to Eq. (46) as a superposition:

$$A_z(x,t) = A_h(x,t) + A_d(x,t). \tag{53}$$

In Eq. (53), $A_h(x,t)$ is the homogeneous solution and $A_d(x,t)$ is the driven solution. We similarly decompose the plasma current density as

$$J_p = -\frac{\sigma}{c}\frac{\partial A_z}{\partial t} = -\frac{\sigma}{c}\left(\frac{\partial A_h}{\partial t} + \frac{\partial A_d}{\partial t}\right) \equiv J_{ph} + J_{pd} \tag{54}$$

and the plasma current as

$$I_p = -\frac{\sigma}{c}\frac{\partial}{\partial t}\int_0^{\ell} dx(A_h + A_d) \equiv I_{ph} + I_{pd}. \tag{55}$$

The homogeneous solution A_h describes the relaxation of the magnetic field which pre-exists before $t = 0$. It is governed by

$$-\frac{c}{4\pi}\frac{\partial^2 A_h}{\partial x^2} = -\frac{\sigma}{c}\frac{\partial A_h}{\partial t} \tag{56}$$

and is subject to the boundary condition

$$A_h(0,t) = A_h(\ell,t) = 0 \tag{57}$$

and to the initial condition

$$A_h(x,0) = (\pi\ell I_b/c)\,(1 - |2x-\ell|/\ell). \tag{58}$$

The driven solution A_d represents the response to the transverse motion of a current source which is "switched on" instantaneously at time $t = 0$. That is, the initial magnetic field plays no role in the driven solution A_d. Thus A_d satisfies

$$-\frac{c}{4\pi}\frac{\partial^2 A_d}{\partial x^2} = -\frac{\sigma}{c}\frac{\partial A_d}{\partial t} + I_b\,\delta(x - x_B(t)) \tag{59}$$

and is subject to the boundary condition

$$A_d(0,t) = A_d(\ell,t) = 0 \tag{60}$$

and to the initial condition

$$A_d(x,0) = 0. \tag{61}$$

Both A_h and A_d may be obtained by the method outlined in Appendix B. Let us first concentrate on A_h. It is given by [cf. Eq. (B15)]

$$A_h(x,t) = \frac{4\ell I_b}{\pi c} \sum_{\substack{n=1 \\ n\ \mathrm{odd}}}^{\infty} \frac{2}{n^2\pi} (-1)^{\frac{n-1}{2}} e^{-n^2(\frac{\pi t}{2\tau_d})} \sin(\frac{n\pi x}{\ell}) \tag{62}$$

which relaxes on the time constant τ_{dif}. A_h also gives rise to J_{ph} which decays on the same time scale. The evolution of J_{ph} is shown in Fig. 3 for two values of v. Its spatial distribution is approximately gaussian. Note that for $t << \tau_{dif}$, $I_{ph} \to I_b$, as expected on physical grounds and readily verified from solution (62). Thus, in the limit $v >> 1$, I_{ph} contributes one unit to the current enhancement factor F.

The driven solution A_d gives rise to the unexpected features mentioned at the beginning of this subsection. It is given by

$$A_d(x,t) = \frac{4\ell I_b}{\pi c} \sum_{n=1}^{\infty} \frac{2}{\pi n(n^2 + v^2)} d_n(t) \sin(\frac{n\pi x}{\ell}) \tag{63}$$

where

$$d_n(t) = n \sin(nh) - v \cos(nh) - e^{-(\frac{n^2 t}{2\tau_{dif}})} [n \sin(nh_o) - v \cos(nh_o)] \tag{64}$$

with $h = \pi(1 + t/\tau_t)/2$ and $h_o = \pi/2$. The evolution of $J_{pd}(x,t)$ is shown in Fig. 4 for $v = 0.5$ and for $v = 4$.

We note that $J_{pd}(x,t)$ is negative for $t/\tau_t << 1$ but becomes positive for $t/\tau_t \to 1$. This behavior may be understood by observing that J_{pd} is the plasma current due to a current source that is switched on at time $t = 0$. Initially, $A_d = 0$. An induced field and current are thus generated at time $t = 0^+$ so as to maintain zero magnetic field by Lenz's law. Initially, I_{pd} exactly cancels I_b, i.e., $I_{pd} \to -I_b$ as $t \to 0^+$. A major portion of the negative inductive electric field lies ahead of the sheet current, especially when $v >> 1$ [cf. Fig. 4]. However, as this inductive electric field "wave front" approaches the conducting boundary P_R, it is reflected and its polarity is changed in the same manner as when a voltage wave is reflected by a short on the path of a transmission line. In this analogy, the transmission line is lossy. But in the limit of high electrical conductivity ($v >> 1$), the reflected current pulse has not decayed substantially, i.e., $I_{pd} \to + I_b$ as $t \to \tau_t$ for $v >> 1$. Hence, $F \to 1$ as $t \to 0$, while $F \to 3$ as $t \to \tau_t$ for $v >> 1$.

In fact, a simple analytic solution for the driven solution A_d and the associated current density J_{pd} may be derived in the limit that $v >> 1$. First, it is easily seen that Eq. (59) admits a wave-like solution of the form $A_d^1(x,t) \propto f[x - x_b(t)]$. Such a solution yields an induced current density given by

$$J_{pd}^1(x,t) = \begin{cases} 0 & ; \quad x < x_b \\ -\left(\frac{\pi I_b v}{\ell}\right) e^{-\pi v(x-x_b)/\ell} & ; \quad x > x_b \end{cases} \tag{65}$$

which is indeed an approximate solution when the current sheet is far from the wall. The important feature is that J_{pd}^1 lies entirely ahead of the beam and thus reaches the wall before the beam. Because $A_d^1(x,t)$ does not satisfy the boundary condition $A_d^1(\ell,t) = 0$, an image current source of the form $-I_b\delta\{x-[2\ell-x_b(t)]\}$ must be added to render the vector potential zero at $x = \ell$. Associated with this image is the plasma current density

$$J_{pd}^{2}(x,t) = \begin{cases} 0 , & x > 2\ell - x_b \\ \left(\frac{\pi I_b v}{\ell}\right) e^{\pi v(x - 2\ell + x_b)/\ell}, & x < 2\ell - x_b \end{cases} \qquad (66)$$

which represents the reflected wave previously mentioned. Summing all currents (I_b, I_{ph}, I_{pd}^{1}, I_{pd}^{2}) between P_L and P_R yields a current enhancement factor of 3 as $x_b \to \ell$, since the contribution from I_{pd}^{1} becomes negligibly small while the contribution from I_{pd}^{2} becomes significant. Equations (65) and (66) demonstrate why current enhancement occurs within a boundary layer of width ℓ/v of P_R.

For simplicity of exposition, the calculations of this section have been based on idealized model assumptions. We now relax some of these assumptions and use the insight provided by our results to predict what happens when the beam has finite thickness or nonuniform velocity to the wall. (One could also draw insight for the case of non-uniform conductivity.) Consider first the neglect of finite beam thickness. Thick beams can be treated as a linear superposition of thin beams. A beam is thin if its thickness 2a is small compared with the skin depth $\delta_o = \ell/\pi v = c^2/4\pi\sigma u$. If the beam is thick, the limiting value of F is reduced because part of the beam is more than one skin depth away from the wall when the beam's leading edge reaches the wall. High current enhancement is thus possible in broad conductivity channels only if

$$a << c^2/4\pi\sigma u << \ell. \qquad (67)$$

Current gains above three are possible in broad channels if the beam accelerates to the wall. To show this, consider a case where x_b maintains uniform motion at speed u until $t = T_1 < \tau_t$, but undergoes an impulse acceleration so that $dx_b/dt = u_1 = \text{constant} (> u)$ for $t > T_1$. For time $t < T_1$, the solution remains the same as that obtained in the previous subsection. Specifically, $F(T_1) > 1$. For time $t > T_1$, since u_1 is uniform, we may again

use the previous section; the only modification is that the solution is time-translated by T_1 and that the "initial condition" at $t = T_1$ must reflect a larger initial current, $F(T_1)I_b$. Now, for $u_1 \to \infty$, we have as $x_b \to \ell$, $F = (I_b + I_{pd} + I_{ph})/I_b = 1 + 1 + (I_{ph}/I_b) = 2 + F(T_1) > 3$. Here, we have used the result that $I_{pd} \to I_b$ irrespective of the "initial condition". In retrospect, it is somewhat surprising that $F \to 3$ regardless of the magnitude of u so long as it is large and constant, but that F may exceed 3 if $du/dt > 0$.

We saw in Sec. 2.2 that the current gain for narrow and stationary conductivity channels is restricted to $F < 2$; this low value of F_{max} occurs because only the beam current I_b physically displaces to lower the inductance L. For the broad channels discussed in this section, F_{max} can be as large as three or more because a portion of the plasma current, I_{pd}, moves with I_b to further lower L. Maximum current gain is achieved if <u>all</u> current moves with I_b so that the final value of $L(\geq 0)$ is minimized. This is the case for a narrow conductivity channel which physically displaces with the beam. In this case, the final values of L and F are limited only by the finite breadth of the beam and channel, which prevents all the net current from simultaneously reaching the boundary. By applying flux conservation to inductance formula (A4) of Appendix A, we conclude that in cylindrical geometry the maximum current gain is given by

$$F_{max} = \frac{\ln(b/a) + \alpha}{\ln(2) + \alpha} \tag{68a}$$

where a is a characteristic beam-channel radius, b is the boundary radius, $\alpha^2 \leq \frac{1}{4}$, and the beam displacement r_b varies from zero to $(b - a)$. Similar arguments applied in planar geometry produce

$$F_{max} = \ell/a \tag{68b}$$

where ℓ is the plate separation and 2a characterizes the thickness of the beam and conductivity sheets. Hose-unstable beams are unlikely, however, to produce current gains much above a factor of two because they leave behind a highly conducting on-axis channel that traps plasma current and magnetic flux; see Sec. 4.1.

The displacement current has been neglected thus far, and in the numerical simulations of the next section as well. While the physical description given here indicates that the displacement current effects should be small, we nevertheless repeated our calculations with the displacement current term $(4\pi c)^{-1}\partial^2 A_z/\partial t^2$ included on the left-hand side of Eq. (46). In addition to conditions (47) and (48), the initial condition $\partial A_z/\partial t = 0$ at $t = 0$ is introduced to completely specify the solution A_z. The current enhancement factor F is calculated according to Eq. (49b) which now implicitly includes the displacement current. The result is shown in Fig. 5. We conclude from Fig. 5 that the displacement current generally increases the enhancement factor F, but that F does not exceed a value of 3.2 if $u/c \leq 0.3$. This explicit demonstration of the unimportance of the displacement current provides additional confidence in Lee's simplified field equations which are used in the simulations presented in Sec. 4.

4. Computational Models

The resistive hose instability has been widely studied using linearized simulation models[14,19,20] which are valid only for small beam displacements. However, the current multiplication effect described in the previous sections is an inherently nonlinear phenomenon. In this section, we describe nonlinear simulations using a new particle code, SARLAC. This code provides a self-consistent treatment of the hose instability for large displacements and reproduces the current enhancement effect. A more complete description of the code is given elsewhere.[21]

SARLAC employs a number of approximations which have been widely used in studies of electron beam propagation. Longitudinal and transverse beam dynamics are decoupled and treated separately (to order $v_\perp/v_z = 2\pi a/\lambda_\beta \ll 1$) by invoking the ultrarelativistic approximation (37) and the paraxial condition (38). The field solver is based on the Lee field equations:[22]

$$\nabla_\perp^2(\tilde{A} + \phi) = -\frac{4\pi}{c}\left(J_b - \sigma\frac{\partial\tilde{A}}{\partial\zeta}\right) \tag{69}$$

and

$$\nabla_\perp^2\frac{\partial\tilde{A}}{\partial\zeta} = \underset{\sim}{\nabla}_\perp\cdot\left(\frac{4\pi\sigma}{c}\underset{\sim}{\nabla}_\perp\phi\right), \tag{70}$$

which are obtained by dropping derivatives of the transverse vector potential ($\frac{\partial}{\partial\zeta}\underset{\sim}{A}_\perp \to 0$) and by employing the frozen-field approximation discussed in Sec. 2.3. Here ϕ is the electrostatic potential, and $\tilde{A} = A_z - \phi$. The independent temporal variable used in SARLAC is not τ but its equivalent, $\zeta = c\tau = ct - z$, which is the distance behind the beam head. The axial electric field is given by

$$E_z = -\frac{\partial}{\partial\zeta}\tilde{A} \tag{71a}$$

while the transverse electric and magnetic fields are given respectively by

$$\underline{E}_\perp = -\underline{\nabla}_\perp \phi \tag{71b}$$

and

$$\underline{B}_\perp = \underline{\nabla}_\perp (\tilde{A} + \phi) \times \hat{z}. \tag{71c}$$

Metallic boundary conditions are assumed:

$$\tilde{A} = \phi = 0 \tag{72}$$

at a specified pipe radius b.

The conductivity σ is treated by a simple rate equation:

$$\frac{\partial \sigma}{\partial \zeta} = KJ_b + \nu_i \sigma/c - \beta_r \rho \sigma^2 \tag{73}$$

where in air we use the beam collisional ionization coefficient $K = 6X10^{-4}$ cm/statamp-sec and the recombination coefficient $\beta_r = 7X10^{-15}$ sec/cm-atm. The gas density ρ is specified in atm. The electron-avalanche ionization rate $\nu_i = \nu_i(\rho;E)$ is a complicated function of density ρ and electric field E, and is given by Eqs. (16) and (17) of Ref. 18.

The beam current density J_b is calculated in the full SARLAC code by accumulating contributions from the simulation particles onto a polar mesh. Since $v_z = c$, all simulation particles remain at constant ζ and move in the transverse plane in response to the fields calculated from Eqs. (69)-(73). Because Eqs. (69)-(73) do not involve derivatives in z and because field information can propagate only forward in ζ, SARLAC is structured differently from conventional simulations. SARLAC treats one ζ-slice at a time, thus

reducing the number of particles in the simulation at any given time to $\sim 10^4$. Each beam slice is propagated forward in z until a specified maximum propagation distance z_{max} is reached; at this point, particles are loaded into the next slice at z = 0, and the process is repeated.

Nonlinear particle simulations similar to SARLAC have been developed by Freeman[23] and Godfrey.[24] The major novel feature of the SARLAC model is its field solver which first does a predictor step using the azimuthally averaged conductivity, followed by two corrector steps. This process is fast and thus allows a large number of Fourier modes to be retained.

4.1 SARLAC Particle Simulations

The SARLAC particle code was designed primarily to treat the nonlinear evolution of the resistive hose instability. Thus, the beam displacements $\bar{X}(\zeta,z)$ and $\bar{Y}(\zeta,z)$ in the full simulation are calculated self-consistently from the particle dynamics. The results below are for a 7 kA, 5 MeV beam with a nominal radius of $a_0 = 1.5$ cm. The beam is injected into a conducting drift tube of radius b = 13.5 cm filled with air at 230 Torr ($p = 0.3$ atm). The beam profile was tapered at injection and had a rise length of $\zeta_r = 210$ cm (7 ns). These parameters closely resemble the ETA experimental parameters reported by Chambers, et al.[5]

Figure 6 is a plot of the beam and net currents, $I_b(\zeta)$ and $I_n(\zeta,z)$, at various propagation distances z. Initially, I_n is everywhere smaller than I_b. As the beam propagates to large z, the value of I_n rises in the beam tail and soon exceeds I_b. At z = 270 cm from injection, the peak net current is 11.5 kA, as compared to $I_b = 6.8$ kA at that point in the beam. The peak net current is thus 70 percent larger than the beam current.

The association of current enhancement with large-amplitude hose motion is shown in Figs. 7 and 8. These figures plot the x and y positions of a subset of simulation particles versus ζ at constant z. As is well-known,[14]

the hose amplitude increases with ζ and (for a while) with z. At z = 130 cm (Fig. 7), the beam displacements are of the order of the beam radius, and current enhancement is not observed. By z = 270 cm (Fig. 8), the hose motion of the beam is highly nonlinear, and the beam is close to striking the wall. For $\zeta \lesssim 500$ cm, the beam radius decreases with ζ as I_n and the resulting pinch force build up. However, in the tail of the beam, the beam expands even though I_n exceeds I_b. This is a nonlinear effect which arises when the beam moves out into regions far from the pipe axis where the fields generated by the front of the beam have fallen off.

The spatial distribution of fields and currents can be seen in contour plots at a fixed point in ζ and z. Figure 9 is a contour plot of the beam current density J_b at ζ = 630 cm and z = 270 cm, showing that the beam has moved close to the drift tube wall. The corresponding plot of conductivity σ in Fig. 10 shows that σ is spread over a much larger area yet still peaks near the pipe axis. Contour plots for the axial electric field E_z are shown in Fig. 11 and display a characteristic two-lobed structure. As the beam spirals counter-clockwise and enters virgin air, it induces a field which drives plasma current opposite to the beam current. As the beam leaves an area, it causes the field to change sign and thus drives plasma current parallel to the beam current. The plasma conductivity is higher in the latter region. Current multiplication results when the integrated current in the forward current lobe exceeds that in the return current lobe. The net current density contours, $J_n = J_b + \sigma E_z$, are shown in Fig. 12. J_n is spread over a larger area than J_b and its centroid generally lies closer to the pipe axis.

The phenomenology seen in this simulation most closely resembles the model in Sec. 2.2 for narrow conductivity channels. Although the conductivity is spread over a large area, it peaks near the pipe axis and is low near the pipe wall. As the beam moves closer to the wall, the boundary-layer effect discussed in Sec. 3 should emerge. Current gains much above a factor of two

are unlikely, however, because the beam is broad and the conductivity is low in the outer regions. SARLAC runs must typically be terminated before the beam strikes the wall because the accuracy of the field solver becomes suspect in this limit.

The simulation results from SARLAC are similar to the ETA experimental results. In particular, appreciable current enhancement is generally observed only after the beam has propagated sufficiently far that large-amplitude hose motion has occurred. Current enhancements as high as 90 percent ($F = 1.9$) were observed on ETA.[3] Recent experiments by Raleigh and Greig[6] have confirmed the correlation between hose displacement and current enhancement through use of a stabilizing solenoidal field. A solenoidal field of several kilogauss greatly reduced beam displacement and eliminated the observed current enhancement. A similar effect was reported by Ipatov, et al.[7]

4.2 Simplified SARLAC Simulations

In this subsection we present results from a simplified version of the SARLAC code. As in the analytic work described in Secs. 2.2 and 3, we do not use self-consistent beam dynamics but instead represent the beam as a rigid structure of constant radius whose vector displacement $\underline{r}_b$ is specified. Unlike the analytic work, however, the simulations do incorporate a self-consistent treatment for the plasma conductivity. The removal of beam dynamics from SARLAC enables us to study the dependence of current enhancement on individual beam and cavity parameters as distinct from the dependence on hose growth in total.

The nominal parameters for this study are: beam current $I_b = 7$ kA, beam duration $\zeta_{max} = 10^3$ cm, beam current rise $\zeta_r = 210$ cm, beam radius $a = 1$ cm, pipe radius $b = 7$ cm, and gas density $\rho = 1$ atm. The beam centroid $\underline{r}_b = (X,Y)$ is taken to be a regular spiral growing linearly in ζ, as discussed in Ref. 14

for hose instability in the beam body: $X(\zeta) = 6 \times 10^{-3}\zeta \sin [7.3 \ln (\zeta/3)]$ and $Y(\zeta) = 6 \times 10^{-3}\zeta \cos [7.3 \ln (\zeta/3)]$, so that the beam displacement distance $r_b(\zeta) = 6 \times 10^{-3}\zeta$. The current enhancement factor $F(\zeta) = I_n(\zeta)/I_b(\zeta)$ is plotted as curve (a) in Fig. 13. Note that current enhancement does not become appreciable until $r_b(\zeta)$ approaches half the wall radius ($\zeta \geq 500$ cm). For a given displacement, the enhancement is smaller than in the previous simulation, due primarily to a smaller displacement velocity $\frac{dr_b}{d\zeta}$.

The theoretical basis developed in Secs. 2 and 3 predicts that current enhancement is a boundary effect arising from magnetic flux compression against either a metallic pipe or the "vacuum conductivity" radius, whichever is smaller. Increasing the boundary radius for a given beam perturbation should therefore reduce the enhancement. This prediction was confirmed by enlarging the pipe radius from 7 cm to 49 cm while keeping the remaining simulation parameters unchanged. As seen in curves (a) and (b) of Fig. 13, F does decrease but not dramatically because the monopole fields now terminate at the vacuum boundary, $b_{vac} = 10$ cm $< b_{pipe} = 49$ cm.

The effect of decreasing the beam radius a from 1 cm to 0.75 cm is shown in curve (c). The effect is small, as expected. The maximum current gain in this case was $F^{(max)} = 1.8$. The fluctuations in F seen at large displacements in Fig. 13 are indications of field-solver difficulty.

An important effect not yet discussed is the polarization state of the hose instability. The circularly polarized hose mode assumed here causes a monotonic increase in the beam displacement distance $r_b(\zeta)$. As a result, the circuit inductance L decreases steadily while the net current I_n smoothly rises. If hose growth were plane polarized (perhaps due to an asymmetric initiation), the displacement r_b, inductance L and net current I_n would oscillate, as seen in Fig. 14 where a beam centroid motion of $X = 0$ and $Y = 3 \times 10^{-3}\zeta \cos [7.3 \ln (\zeta/3)]$ was imposed. A typical experiment produces random hose polarizations, and hence I_n should increase more or less steadily but with some irregular fluctuations.

5. Conclusion

We have shown that current enhancement is a natural consequence of the resistive hose instability for electron beams propagating in dense gases. The degree of enhancement depends on the displacement amplitude of the beam relative to the boundary radius where the monopole electric field E_{zo} falls to zero. The boundary radius is usually determined by the ground returns (e.g., metallic drift tube) present in most experiments. If the return-current structures are far from the beam, current enhancement still occurs but the boundary radius is determined by the location where beam-generated conductivity becomes vanishingly small.

The physical basis for current enhancement is conservation of magnetic flux. As a beam displaces off axis, it lowers the effective inductance. The circuit responds by raising the net current so as to conserve magnetic flux (or energy) within the conducting plasma. Enhancement takes place provided the beam displaces within a monopole time $\tau_o = L/R$ where L is the circuit inductance and R is the plasma resistance.

The plasma eddy currents which produce current enhancement also drive the hose instability. The hose instability develops on a plasma dipole decay time τ_d. Large hose growth is therefore possible in a monopole time $\tau_o \gg \tau_d$. Beams undergoing large-amplitude hose motion are thus apt to produce substantial current enhancement. Note that the hose instability, in contrast to the two-stream instability,[1] produces current enhancement regardless of the sign of the beam charge. A positive-ion beam undergoing hose motion would thus induce electric fields that again raise the net current.

Net currents as large as three times the beam current or more are possible if the plasma conductivity extends out to the boundary radius. In practice, the current gain rarely exceeds a factor of two, due both to the

restricted distribution of plasma conductivity and to the finite size of the beam. Our particle simulation results showed current enhancements of ~ 70 percent, which is in good agreement with the ETA experimental results.

Acknowledgments

We are particularly grateful to Dr. Frank W. Chambers and his colleagues at Lawrence Livermore National Laboratory for sharing and describing in detail the ETA experimental results on current enhancement, and for sharing their ideas about the origin of the phenomenon. We additionally thank Dr. Michael Raleigh and Dr. J. Robert Greig for discussing their experimental results prior to publication. The comments of Dr. Steven P. Slinker regarding current enhancement due to axisymmetric instabilities and the assistance of Mr. Paul Boris in preparing the contour plots are appreciated as well.

This work was supported by the Defense Advanced Research Projects Agency under ARPA Order No. 4395, Amendment No. 54, and monitored by the Naval Surface Weapons Center.

Appendix A: Inductance Formulae

We present without derivation some inductance formulae for several different configurations. These formulae when inserted into circuit equation (14) enable one to compute the net current for a prescribed beam perturbation. The maximum current enhancement resulting from sudden displacement of a beam outside an on-axis plasma channel is given as an example.

The inductance for an on-axis beam and plasma of characteristic radius a is given from Eq. (15) by

$$L = \frac{2}{c^2}\,[\ell n(b/a) + \alpha] \tag{A1}$$

where b is the pipe radius and α is a parameter that depends on the detailed spatial distribution of the plasma conductivity and net current. Typically,

$$\alpha^2 \leq \frac{1}{4}. \tag{A2}$$

If the beam and plasma channel expand self-similarly, the parameter $\dot{L}$ in circuit equation (14) should be set to

$$\dot{L} = \frac{1}{2}\,\frac{\partial L}{\partial t}. \tag{A3}$$

For a beam and conductivity channel of radius a which are displaced off-axis to a location r_b,

$$L = \frac{2}{c^2}\,[\ell n(\frac{b^2 - r_b^2}{ab}) + \alpha]. \tag{A4}$$

Although the conductivity in this case is not azimuthally symmetric about the pipe center (unless $r_b = 0$), Eq. (14) nonetheless remains a reasonable approximation. If the current carriers in the conductivity channel physically displace with the beam, one should set

$$L = \frac{\partial L}{\partial t}. \tag{A5}$$

Otherwise, Eq. (A3) should be used. An example of the latter application is an ionized channel consisting of plasma electrons and ions that do not move laterally but are created by the beam and then destroyed by recombination as the beam moves outward.

If only the beam is displaced while the conductivity channel remains on axis, we can use Eq. (10) to compute a channel self-inductance given by

$$L_p = \frac{2}{c^2} [\ell n(b/a) + \alpha], \tag{A6}$$

and a beam-channel mutual inductance given by

$$L_b = \frac{2}{c^2} [\ell n(b/\tilde{r}_b) + \alpha'] \tag{A7}$$

where in general $\alpha' \neq \alpha$ and where

$$\tilde{r}_b = \text{Maximum } \{a; r_b\}. \tag{A8}$$

Equation (10) can then be rewritten as

$$L_p \frac{\partial}{\partial t} (I_n - I_b) + \frac{\partial}{\partial t} (L_b I_b) = - (I_n - I_b)R. \tag{A9}$$

For sudden displacement of a beam outside an on-axis plasma channel of constant radius a, circuit equation (A9) reduces to conservation of magnetic flux:

$$\delta[L_p(I_n - I_b) + L_b I_b] = 0. \tag{A10}$$

If we ignore the usually modest changes in α and α', relationship (A10) when coupled to inductance formulae (A6) and (A7) yields

$$[\ell n(b/a) + \alpha]\ (I_n - I_{no}) = \ell n(r_b/a) I_b. \tag{A11}$$

The maximum possible current gain is therefore given by

$$F = I_n/I_b$$

$$= F_o + \frac{\ell n(r_b/a)}{\ell n(b/a) + \alpha} \tag{A12}$$

where $F_o = I_{no}/I_b$ is the current gain prior to beam displacement. If the displacement occurs rapidly compared with a plasma dipole decay time τ_d, the driven plasma current resides on the plasma surface and the parameter α in Eq. (A12) should be set to zero. For slower displacements, α is unequal to zero. Observe that approximation (A10), and hence result (A12), is valid only if the displacement occurs rapidly compared with a monopole decay time, $\tau_o = L_p/R$. See also the time-dependent solution given in Ref. 10.

Inductance formulae can be formally given for broad conductivity channels but are generally of little practical value. For example, for uniform σ the distribution of plasma conductance is given by

$$\hat{\zeta}(r) = (r/b)^2. \tag{A13}$$

Inductance definition (15) then reduces to

$$L = \frac{2}{c^2} \int_0^b \frac{dr\ r}{b^2}\ \hat{I}$$

$$= \frac{1}{c^2} (1 - \overline{r_n^2}/b^2) \tag{A14}$$

where the mean-square centroid of the net current is given by

$$\overline{r_n^2} = \int_0^b dr\ r^2\ \frac{\partial \hat{I}}{\partial r}. \tag{A15}$$

Inductance formulae for the planar geometries considered in Sec. 3 are similarly straightforward. Unfortunately, these expressions depend strongly on the spatial distribution of the electric field which can be determined only after a full field analysis. A circuit analysis is then unnecessary and superfluous.

Appendix B: Solution to Equation (46)

In this appendix, we derive the solution to Eq. (46) via Fourier analysis. Since the current enhancement factor F is independent of I_b, we set $4\ell I_b/c\pi = 1$ and introduce the dimensionless variables $\xi = \pi x/\ell$ and $\tau = \pi t/2\tau_{dif}$ to normalize Eqs. (46)-(48) as

$$-\frac{\partial^2 A_z}{\partial \xi^2} + \frac{\partial A_z}{\partial \tau} = \delta(\xi - h(\tau)); \quad 0 < \xi < \pi, \; 0 < \tau < \frac{\pi}{2v} \tag{B1}$$

$$A_z(0,\tau) = A_z(\pi,\tau) = 0 \tag{B2}$$

$$A_z(\xi,0) = (\pi/4)\,[1 - |\,2\xi - \pi|/\pi]. \tag{B3}$$

In Eq. (B1),

$$h(\tau) = \frac{\pi}{2} + v\tau \tag{B4}$$

where v is the dimensionless velocity defined in Eq. (51) of the main text and τ_{dif} is the characteristic diffusion time.

Representing the solution as a Fourier series

$$A_z(\xi,\tau) = \sum_{n=1}^{\infty} a_n(\tau) \sin n\xi, \tag{B5}$$

we note that the boundary condition (32) is automatically satisfied and that the initial condition (B3) yields

$$a_n(0) = \frac{1}{\pi}\int_0^{\pi} d\xi A_z(\xi,0) \sin n\xi = \frac{2}{n^2\pi} \sin\left(\frac{n\pi}{2}\right). \tag{B6}$$

Upon substituting (B5) into (B1), we obtain an equation for $a_n(\tau)$:

$$\frac{\partial a_n(\tau)}{\partial \tau} + n^2 a_n(\tau) = \frac{2}{\pi} \sin\left[\frac{n\pi}{2} + nv\tau\right] \tag{B7}$$

which may be easily integrated to yield

$$a_n(\tau) = \frac{2}{\pi} \frac{1}{n^2(n^2 + v^2)} \{ n^2 \sin nh - nv \cos nh + e^{-n^2\tau}$$

$$(v^2 \sin nh_o + nv \cos nh_o)\} \tag{B8}$$

where h is defined in (B4) and $h_o = \pi/2$. The initial condition (B6) has been used to obtain (B8).

The current enhancement factor F is given by [cf. (49b)]:

$$F(\tau) = + \frac{\partial A_z}{\partial \xi}\bigg|_{\xi=0} - \frac{\partial A_z}{\partial \xi}\bigg|_{\xi=\pi} = 2 \sum_{\substack{n=1 \\ n\ \text{odd}}}^{\infty} n a_n(\tau) \tag{B9}$$

where we have used (B5) to obtain the last expression. Some care is to be exercised in evaluating the infinite sum since the first term in the curly bracket of (B8) contributes to a nonuniformly convergent series in (B9). To remove this nonuniform convergence, let us write

$$2 \sum_{\substack{n=1 \\ n\ \text{odd}}}^{\infty} \left\{\frac{2}{\pi} \frac{n^2 \sin nh}{n(n^2 + v^2)}\right\} = \frac{4}{\pi} \sum_{\substack{n=1 \\ n\ \text{odd}}}^{\infty} \left(\frac{1}{n} - \frac{v^2}{n(n^2 + v^2)}\right) \sin nh$$

$$= 1 - \frac{4}{\pi} \sum_{\substack{n=1 \\ n\ \text{odd}}}^{\infty} \frac{v^2}{n(n^2 + v^2)} \sin nh \tag{B10}$$

where we have used the identity

$$\frac{4}{\pi}\left[\sin h + \frac{\sin 3h}{3} + \frac{\sin 5h}{5} + \cdots\right] = 1; \quad 0 < h < \pi. \tag{B11}$$

Note that the infinite series in (B11) is nonuniformly convergent, but converges in a point-wise manner for all h in the open interval $(0,\pi)$. We now substitute (B8) into (B9), and use (B10) to write

$$F(\tau) = 1 + \frac{4}{\pi}\sum_{\substack{n=1\\ n\ \text{odd}}}^{\infty} \frac{1}{n(n^2+v^2)}\left\{-v^2\sin nh - nv\cos nh + e^{-n^2\tau v^2}\sin\left(\frac{n\pi}{2}\right)\right\} \tag{B12}$$

which may readily be compared with Eq. (52) in the main text. The infinite series in (B12) is absolutely and uniformly convergent. As the current sheet is about to touch the conducting plate, $\tau \to \pi/2v$, $h \to \pi$, and Eq. (B12) yields

$$F \to 1 + \frac{4}{\pi}\sum_{\substack{n=1\\ n\ \text{odd}}}^{\infty} \frac{v}{n^2+v^2} + \frac{4}{\pi}\sum_{\substack{n=1\\ n\ \text{odd}}}^{\infty} \frac{(-1)^{\frac{n-1}{2}} v^2 e^{-n^2\frac{\pi}{2v}}}{n(n^2+v^2)} \tag{B13}$$

which is reproduced as Eq. (50) in the main text upon using the identity

$$\tanh\left(\frac{\pi v}{2}\right) = \frac{4}{\pi}\sum_{\substack{n=1\\ n\ \text{odd}}}^{\infty} \frac{v}{n^2+v^2}. \tag{B14}$$

This identity may be established by a standard technique of complex analysis.

Clearly, the method detailed in this appendix may readily be used to construct the homogeneous solution A_h and the driven solution A_d, as suggested in Sec. 3. For example, the homogeneous solution A_h is obtained by setting the right-hand members of Eqs. (B1) and (B7) equal to zero. Then, (B5) - (B7) yield

$$A_h = \sum_{n=1}^{\infty} a_n(0) e^{-n^2 \tau} \sin n\xi \qquad (B15)$$

which is rewritten as Eq. (53) of the main text upon using (B6). The driven solution A_d may be obtained similarly.

Appendix C: Extension to Two Dimensions

In this appendix we demonstrate the insensitivity of the current enhancement mechanism to geometry by extending the analysis of Sec. 3 to two dimensions. We also demonstrate that our results are insensitive to the initial location of the electron beam for $v \gg 1$.

Consider an infinitesimally thin current-carrying filament ("wire") situated in a square channel of side length ℓ, inside of which the medium is characterized by a constant, uniform electrical conductivity. We again assume that the wire sits inside the channel for a sufficiently long time prior to $t = 0$ that a steady magnetic field is already established at $t = 0$. For $t > 0$, the wire is given a uniform x-ward velocity u.

In terms of the normalized variables outlined in Appendix B, the above system is described by the vector potential $A_z(\xi,\eta,\tau)$ whose evolution is governed by

$$-\frac{\partial^2 A_z}{\partial \xi^2} - \frac{\partial^2 A_z}{\partial \eta^2} + \frac{\partial A_z}{\partial \tau} = \delta\big(\xi - h(\tau)\big)\,\delta(\eta - \eta_o),$$

$$0 < \xi < \pi,\ 0 < \eta < \pi,\ \tau > 0 \qquad \text{(C1)}$$

where ξ,η are the normalized spatial (x,y) variables and $\tau = \pi t/2\tau_{dif}$ as before. The initial coordinates of the wire are $(\xi,\eta) = (h_o, \eta_o)$. For $\tau \geq 0$, we assume

$$h(\tau) = h_o + v\tau \qquad \text{(C2)}$$

and the instantenous coordinates of the wire are $(\xi,\eta) = (h,\eta_o)$. To demonstrate the insensitivity to the geometry, we let h_o, η_o be arbitrary in

this appendix. [Of course, h_o, η_o, h, ξ, η are all restricted to lie between 0 and π]. Equation (C1) is subject to the boundary conditions

$$A_z(0,\eta,\tau) = A_z(\pi,\eta,\tau) = A_z(\xi,0,\tau) = A_z(\xi,\pi,\tau) = 0 \qquad (C3)$$

and to the initial condition

$$A_z(\xi,\eta,0) = \sum_{n=1}^{\infty}\sum_{m=1}^{\infty} \frac{4}{\pi^2}\left(\frac{1}{n^2+m^2}\right) \sin nh_o \sin m\eta_o \sin n\xi \sin m\eta \qquad (C4)$$

which reflects that a steady magnetic field is already established at $\tau = 0$.

The solution to Eq. (C1) may be represented as a Fourier series

$$A_z(\xi,\eta,\tau) = \sum_{n=1}^{\infty}\sum_{m=1}^{\infty} a_{mn}(\tau) \sin n\xi \sin m\eta. \qquad (C5)$$

In so doing, the boundary conditions given in (C3) are automatically satisfied. Upon substituting (C5) into (C1), we obtain the first-order ordinary differential equation for $a_{mn}(\tau)$:

$$\frac{\partial a_{mn}(\tau)}{\partial \tau} + (m^2+n^2)a_{mn}(\tau) = \frac{4}{\pi^2} \sin nh(\tau) \sin m\eta_o \qquad (C6)$$

which may easily be solved upon substituting (C2) into (C6) and using the initial condition

$$a_{mn}(0) = \frac{4}{\pi^2(n^2+m^2)} \sin nh_o \sin m\eta_o. \qquad (C7)$$

The current enhancement factor is

$$F(\tau) = 1 - \frac{\partial}{\partial \tau}\int_0^{\pi}\int_0^{\pi} d\xi d\eta A_z(\xi,\eta,\tau) \qquad (C8)$$

which may also be expressed as

$$F(\tau) = \sum_{\substack{m=1 \\ m,n \text{ odd}}}^{\infty} \sum_{n=1}^{\infty} \frac{4(n^2 + m^2)}{nm} a_{mn}(\tau). \qquad (C9)$$

The last expression is analogous to Eq. (B9). The non-uniform convergence in the infinite series may be handled in a similar manner as in Eq. (B10).

Equation (C9) may be used to calculate the current enhancement factor as the wire is about to reach the side $\xi = \pi$, [i.e., $h \to \pi$]. This limiting value of F is shown in Fig. 15 as a function of the normalized velocity v for various combinations of the initial coordinates (h_o, η_o). Note the insensitivity to (h_o, η_o) and the similarity between the curves in Fig. 15 and that on Fig. 1. Thus, the limiting value of $F \to 3$ is established. We have also shown that the evolution of $F(\tau)$, as governed by (C9), is similar to Fig. 2. Coupled with the interpretation given in Sec. 3.2, we may conclude that the much simpler one-dimensional model provides a sound physical description for current enhancement.

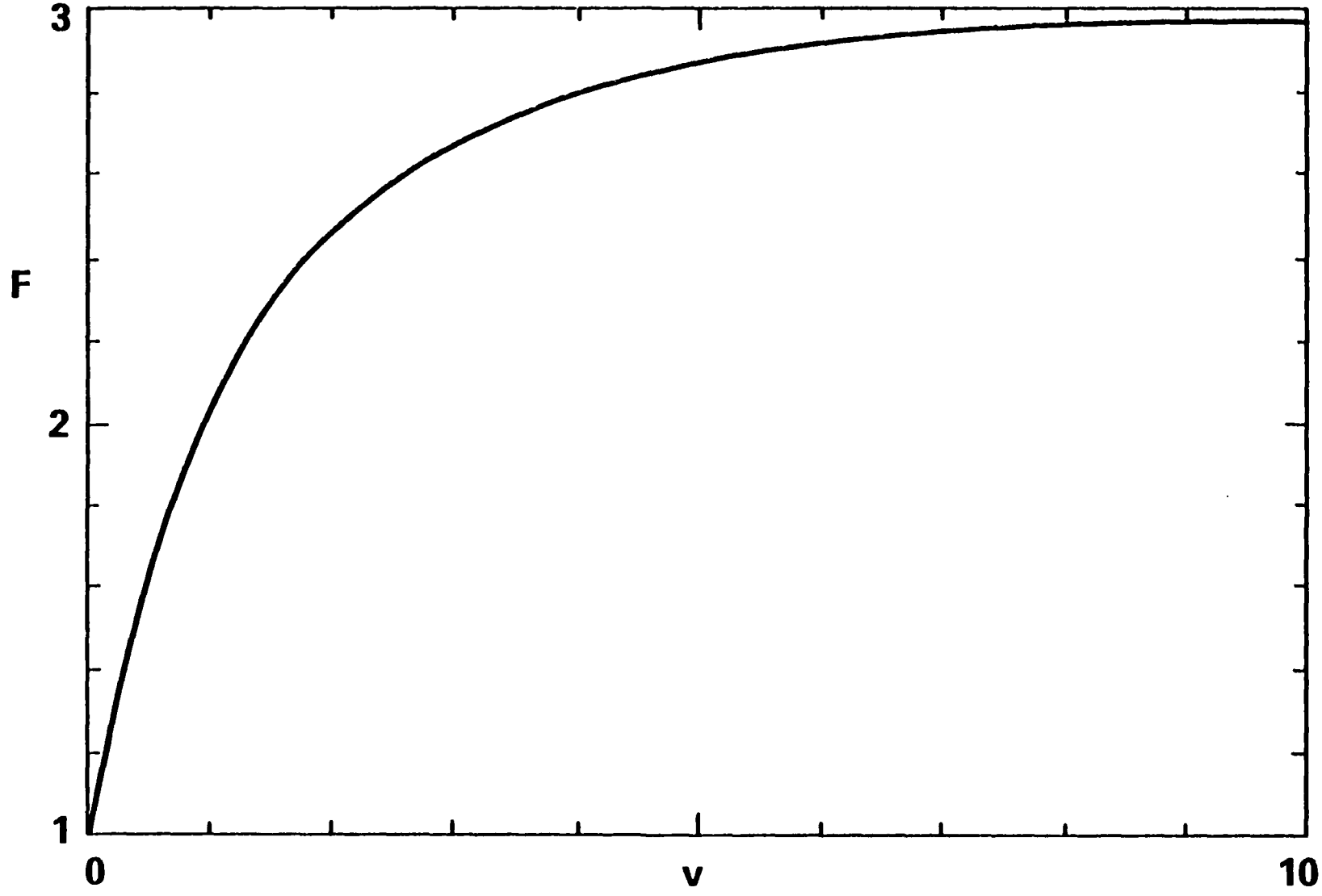

Figure 1: Current gain F just before the current source touches the conducting boundary as a function of normalized velocity v.

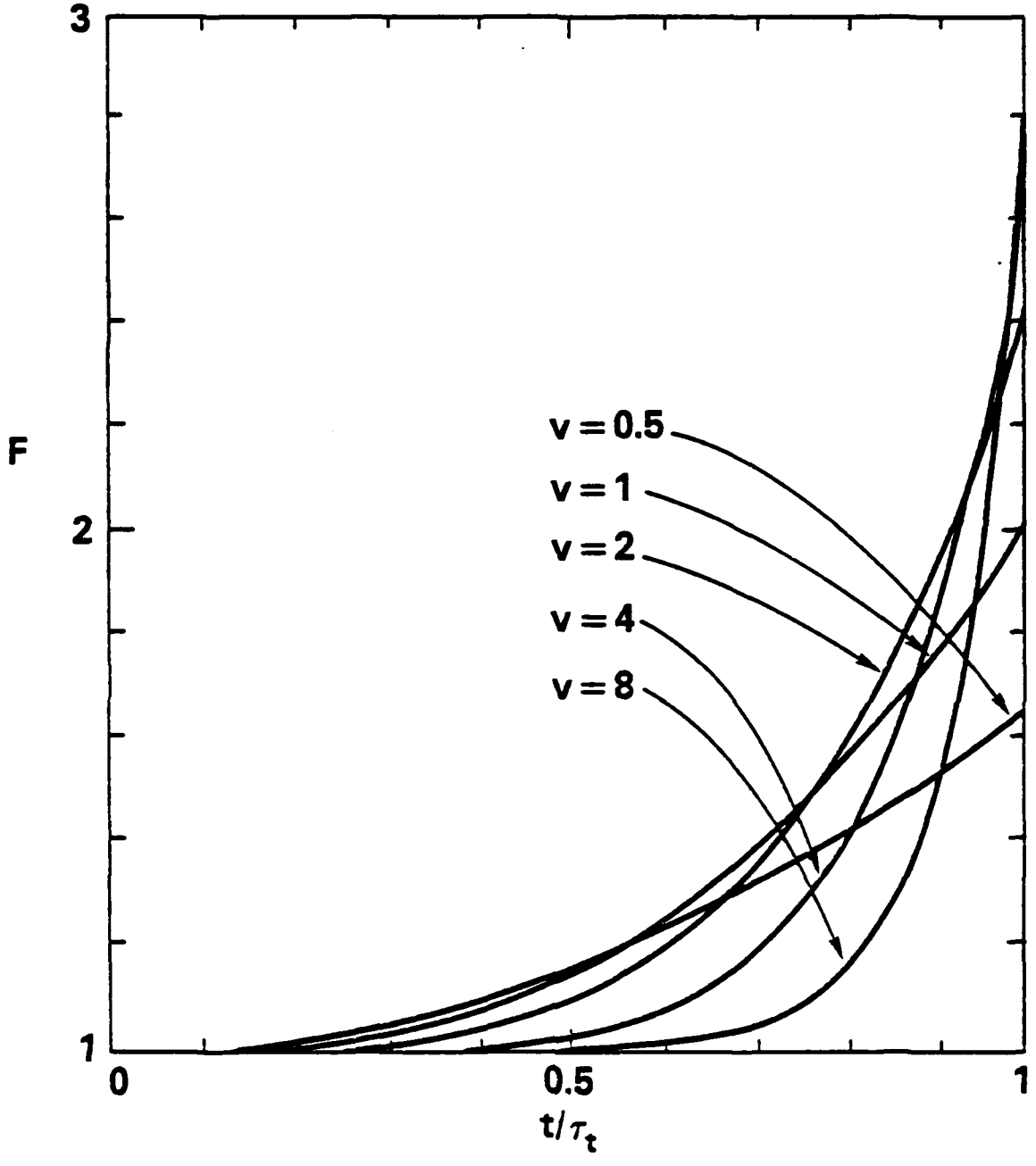

Figure 2: Evolution of F for various values of v.

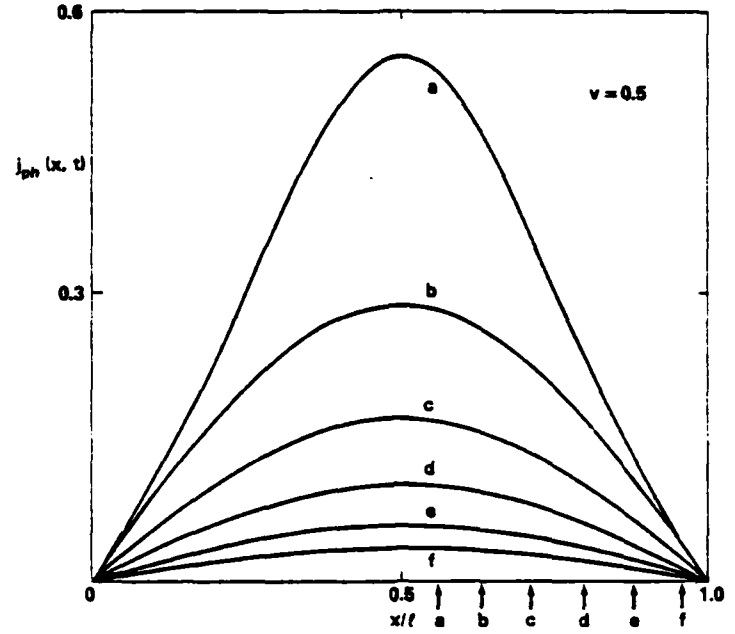

(a)

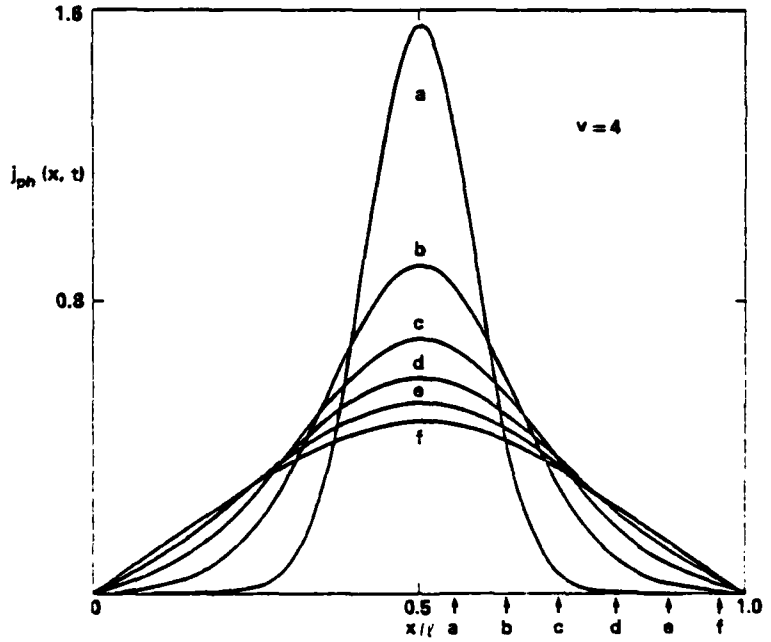

(b)

Figure 3: Evolution of the homogeneous current density J_{ph}, in units of $c\pi I_b/4\ell^2$, for v = 0.5 and v = 4. The arrows at the bottom mark the instantaneous location of the current source for each of the indicated curves.

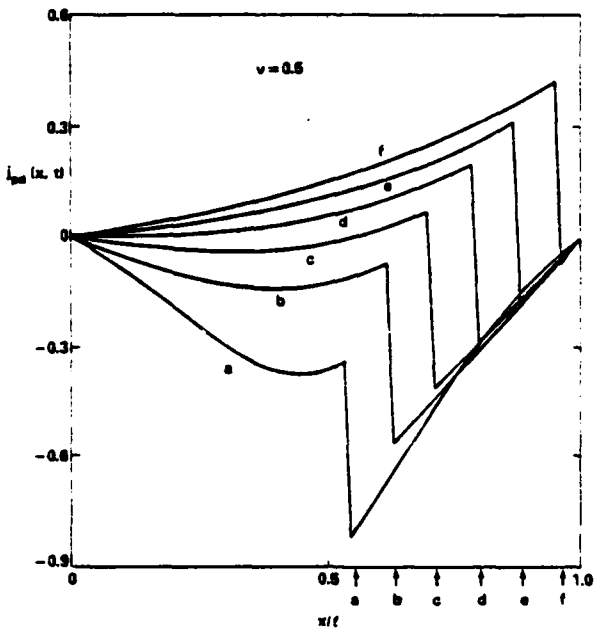

(a)

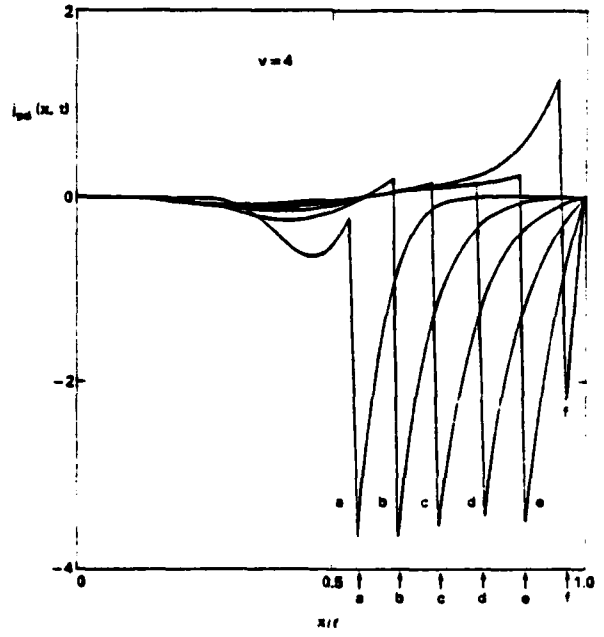

(b)

Figure 4: Evolution of the driven current density J_{pd}, in units of $c\pi I_b/4\ell^2$, for v = 0.5 and v = 4. The arrows at the bottom mark the instantaneous location of the current source for each curve.

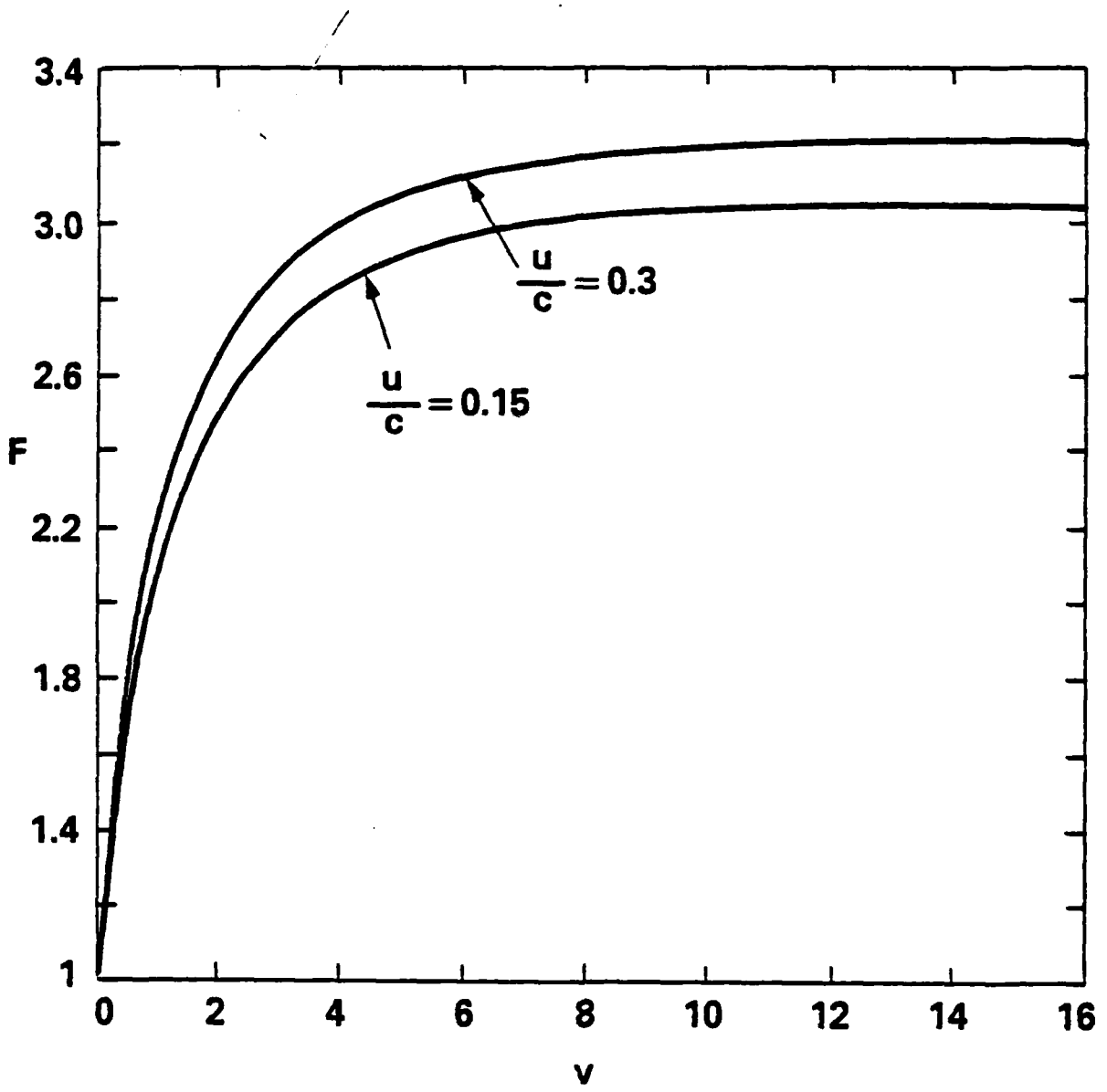

Figure 5: The effect of displacement current on the asymptotic current gain F as a function of v.

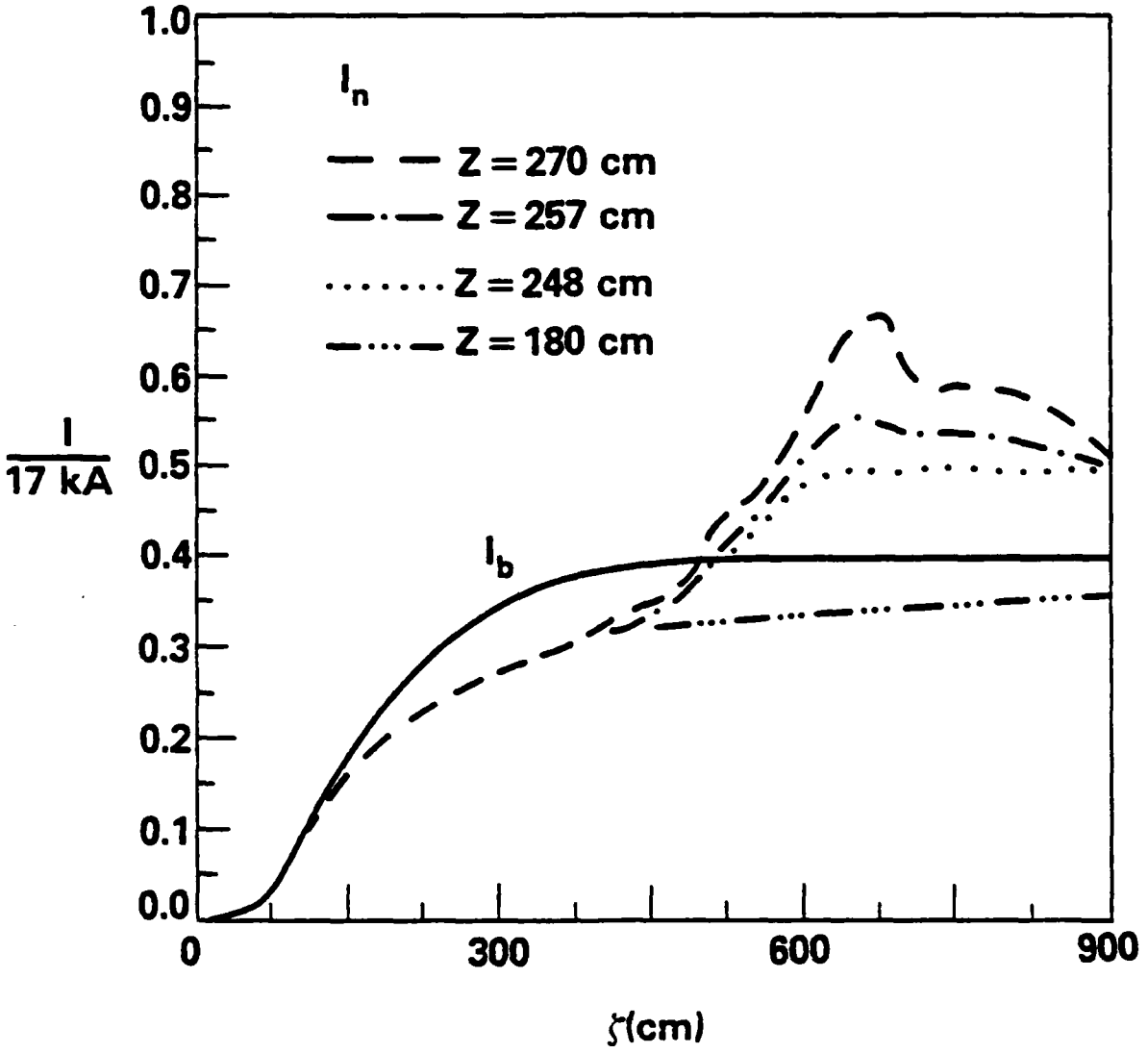

Figure 6: Beam current $I_b(\zeta)$ and net current $I_n(\zeta,z)$ as a function of distance ζ behind the beam head and propagation distance z, for the SARLAC particle simulation described in Sec. 4.1.

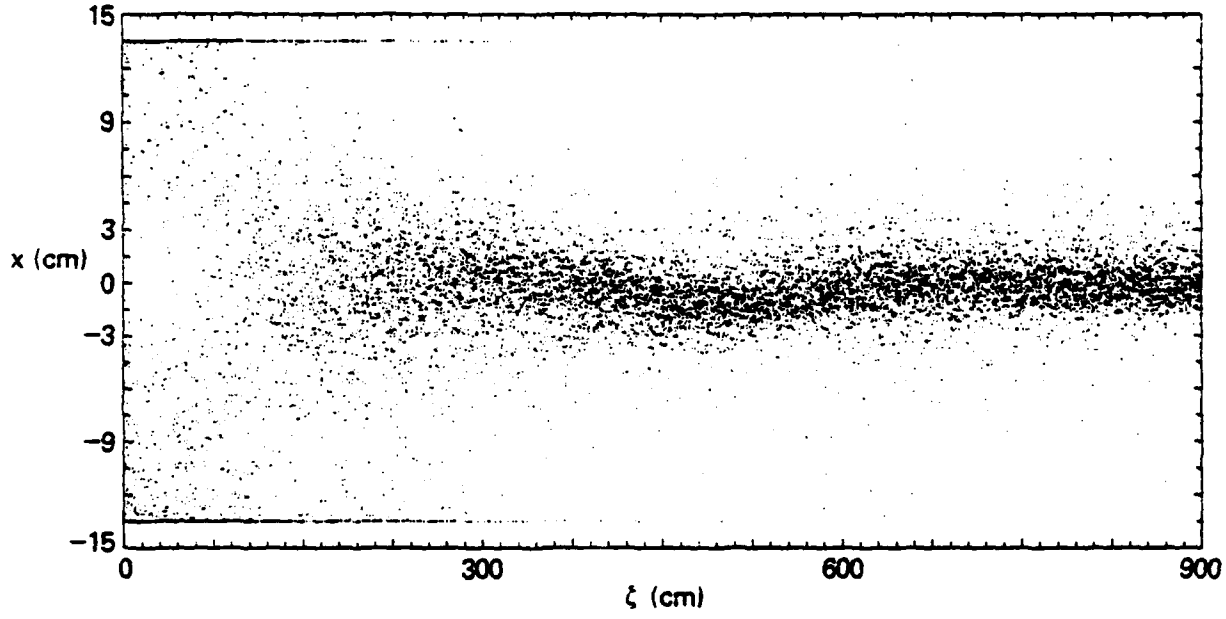

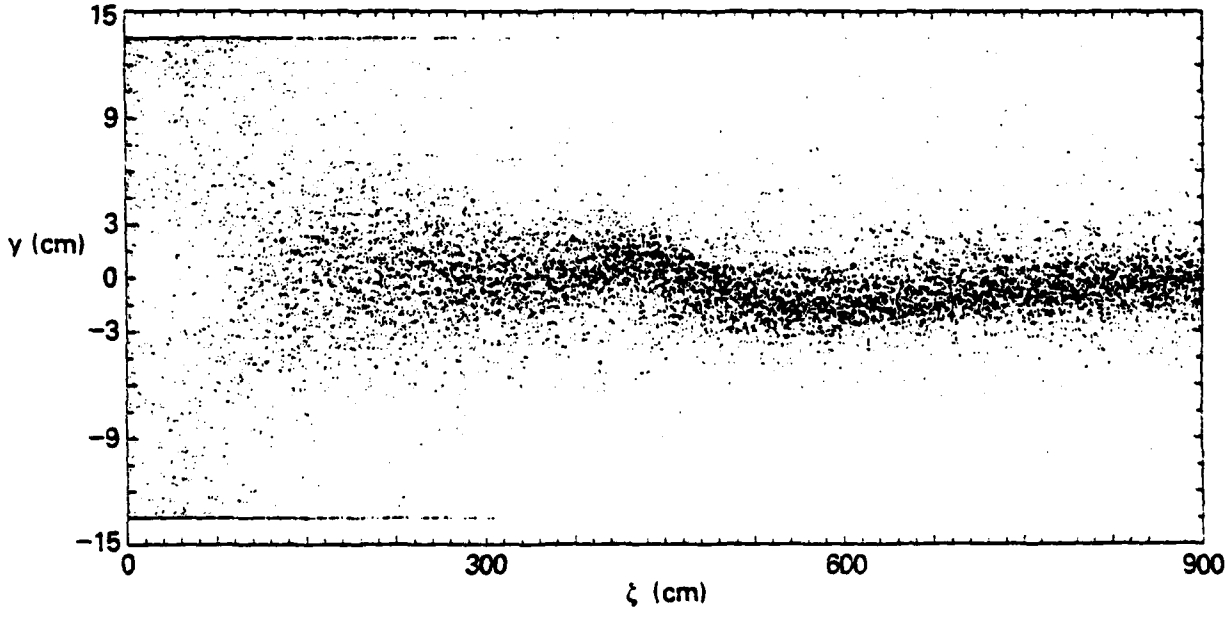

Figure 7: Positions $x(\zeta)$ and $y(\zeta)$ for a subset of simulation particles after propagating $z = 180$ cm.

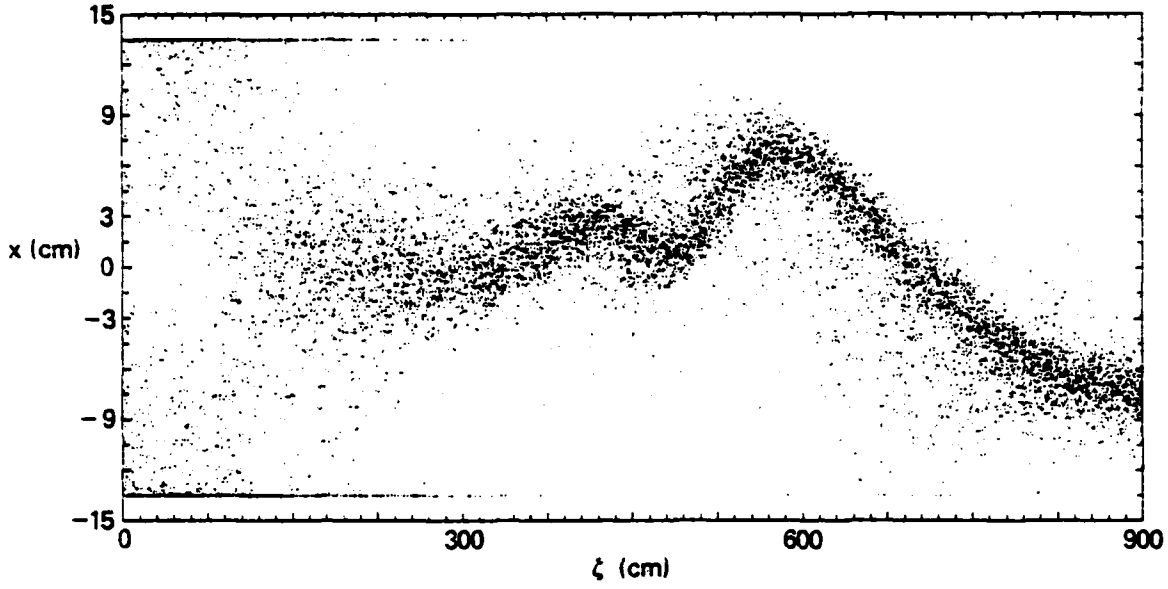

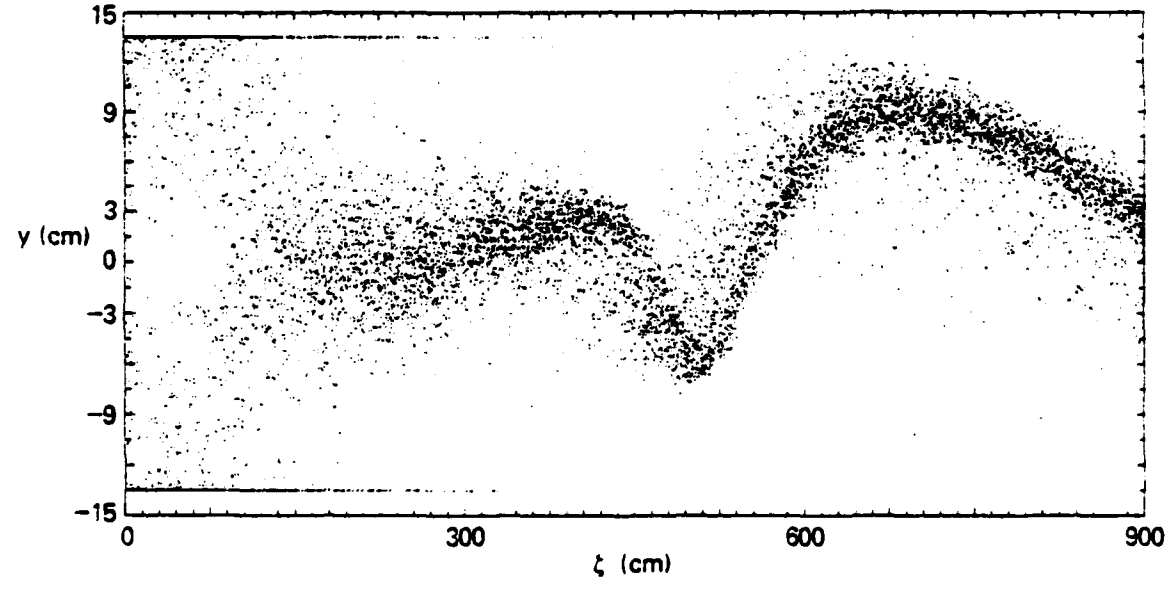

Figure 8: Positions $x(\zeta)$ and $y(\zeta)$ after propagating $z = 270$ cm.

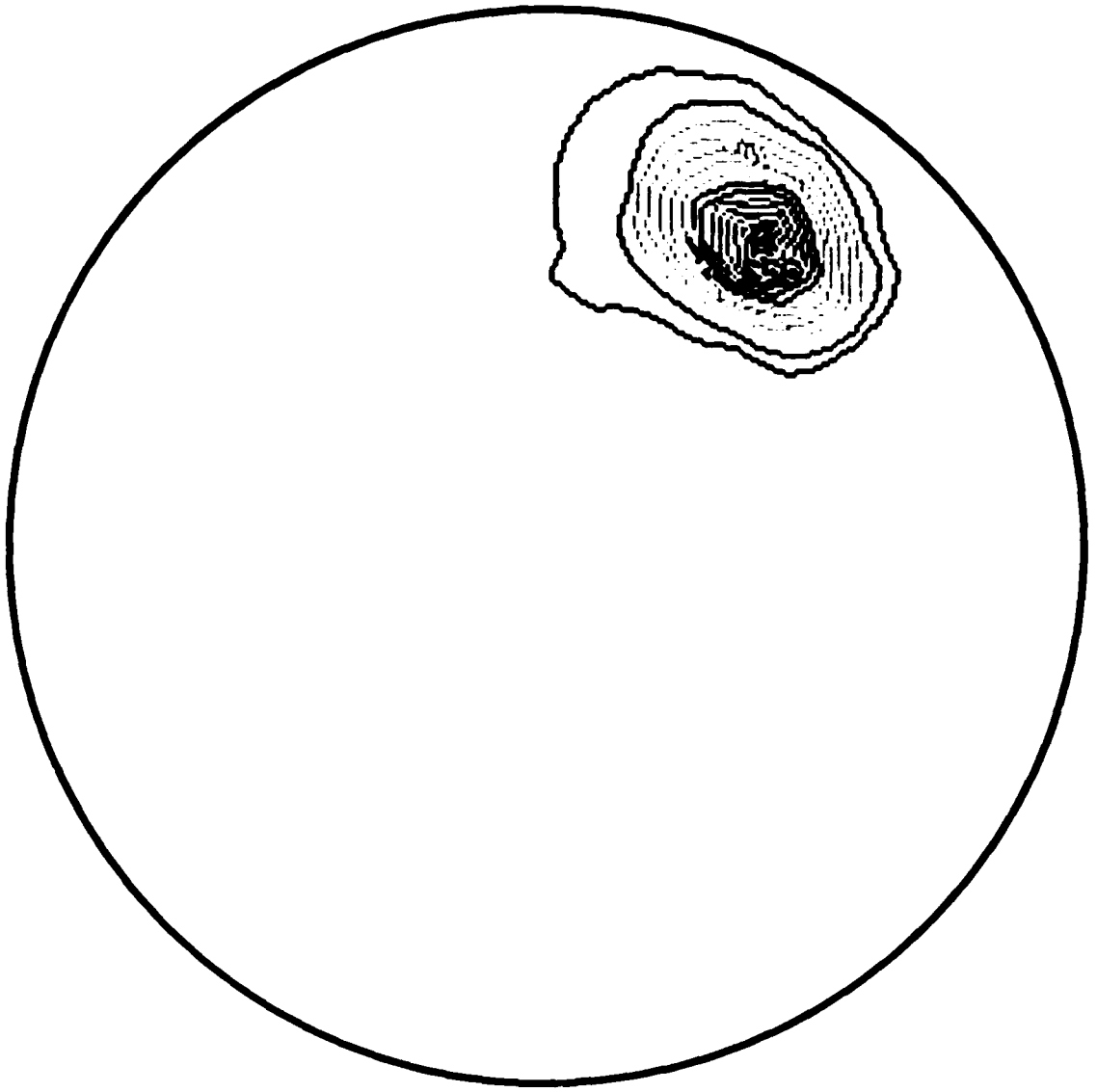

Figure 9: Contour plot of the beam current density $J_b(r,\theta)$, in units of $mc^3/4\pi a_o^2 e$, at ζ = 630 cm and z = 270 cm. The heavy black circle marks the metallic pipe boundary at radius b = 7 cm.

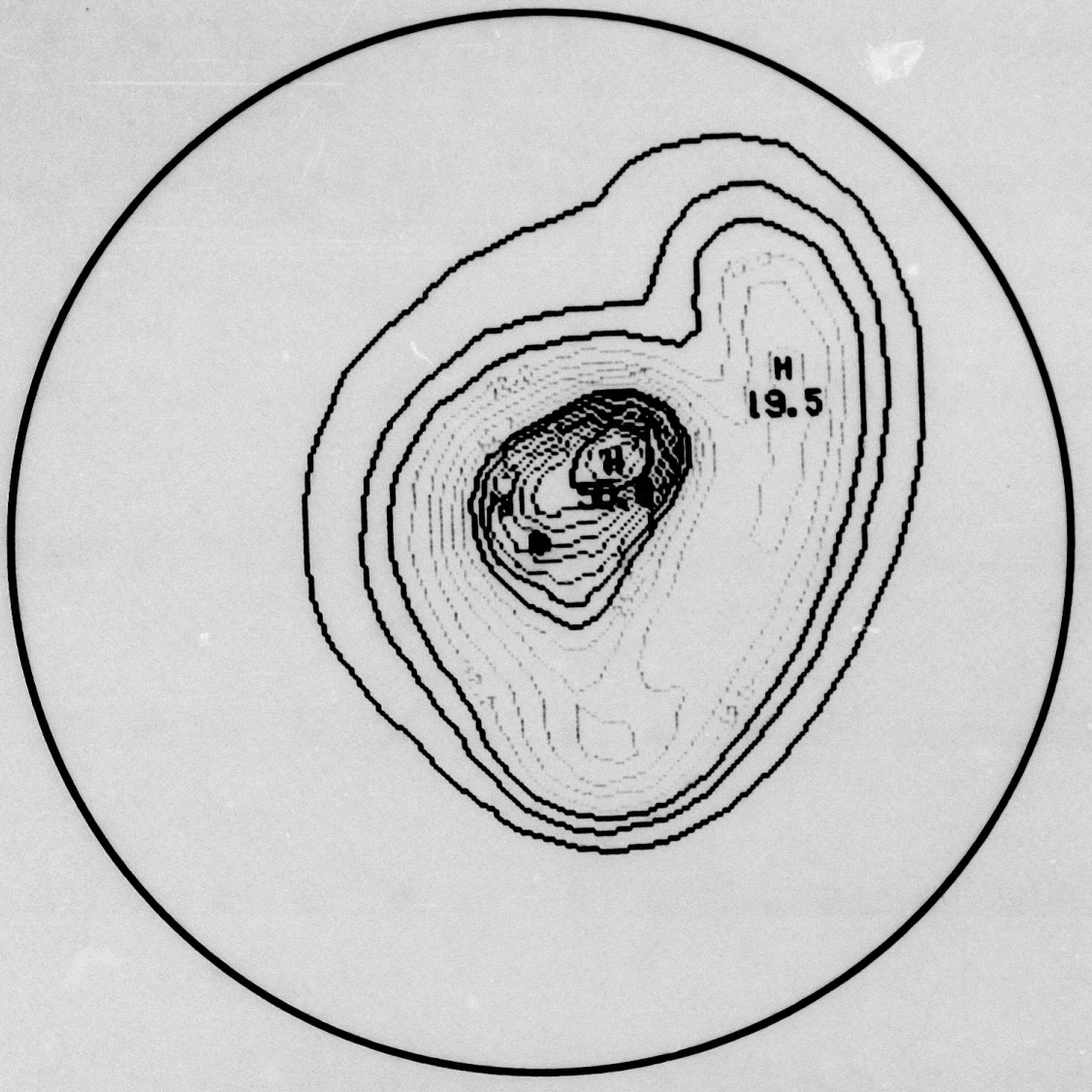

Figure 10: Contour plot of the conductivity $\sigma(r,\theta)$, in units of $c/4\pi a_o$, at ζ = 630 cm and z = 270 cm.

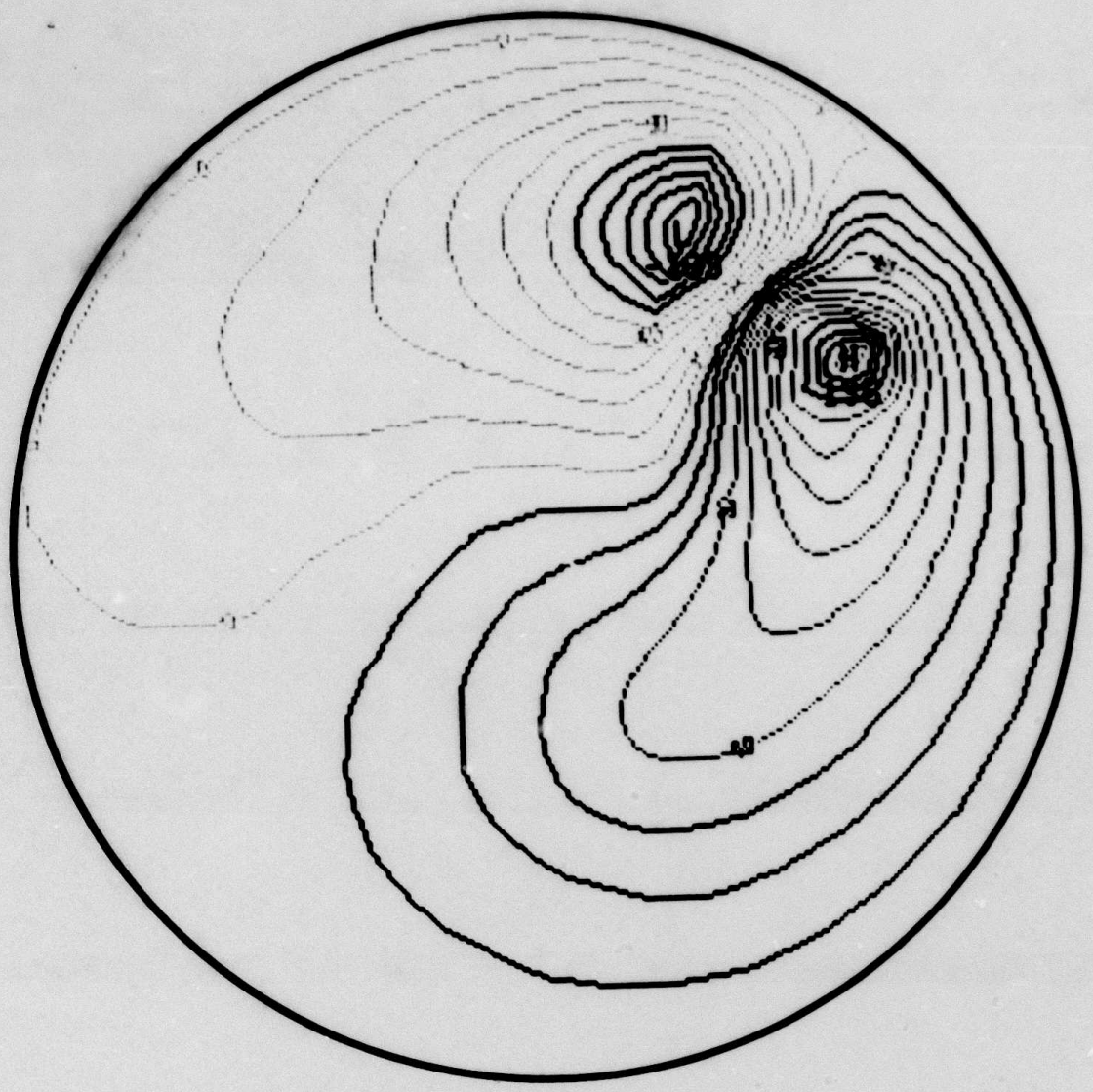

Figure 11: Contour plot of the axial electric field $E_z(r,\theta)$, in units of mc^2/ea_o, at ζ = 630 cm and z = 270 cm. The red and yellow contours define regions where E_z drives return plasma current ($\sigma E_z/J_b < 0$) while the green, blue, and violet contours are where E_z drives forward plasma current ($\sigma E_z/J_b > 0$).

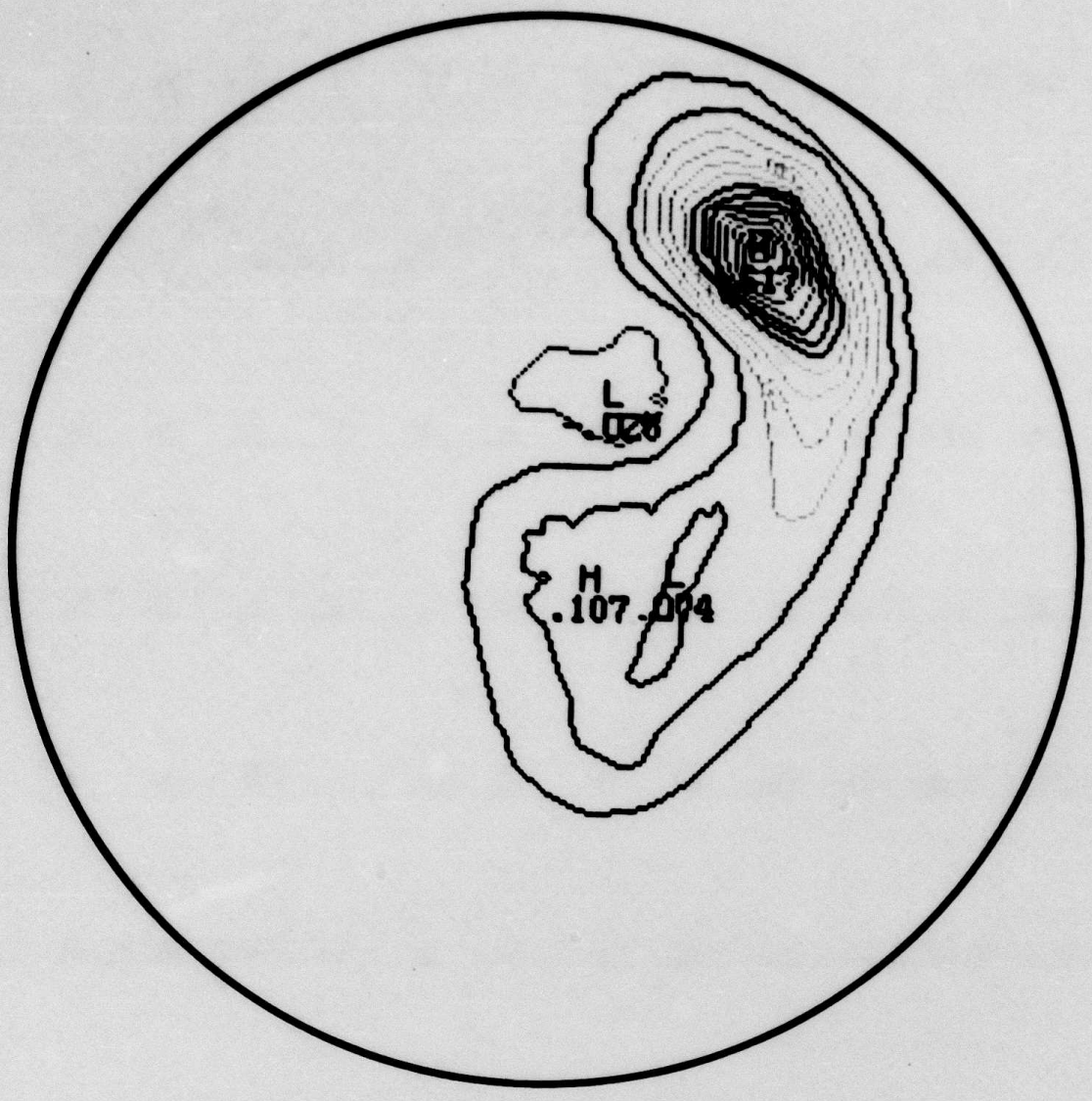

Figure 12: Contour plot of the net current density $J_n(r,\theta)$, in units of $mc^3/4\pi a_o^2 e$, at ζ = 630 cm and z = 270 cm. In almost all regions, $J_n/J_b \geq 0$.

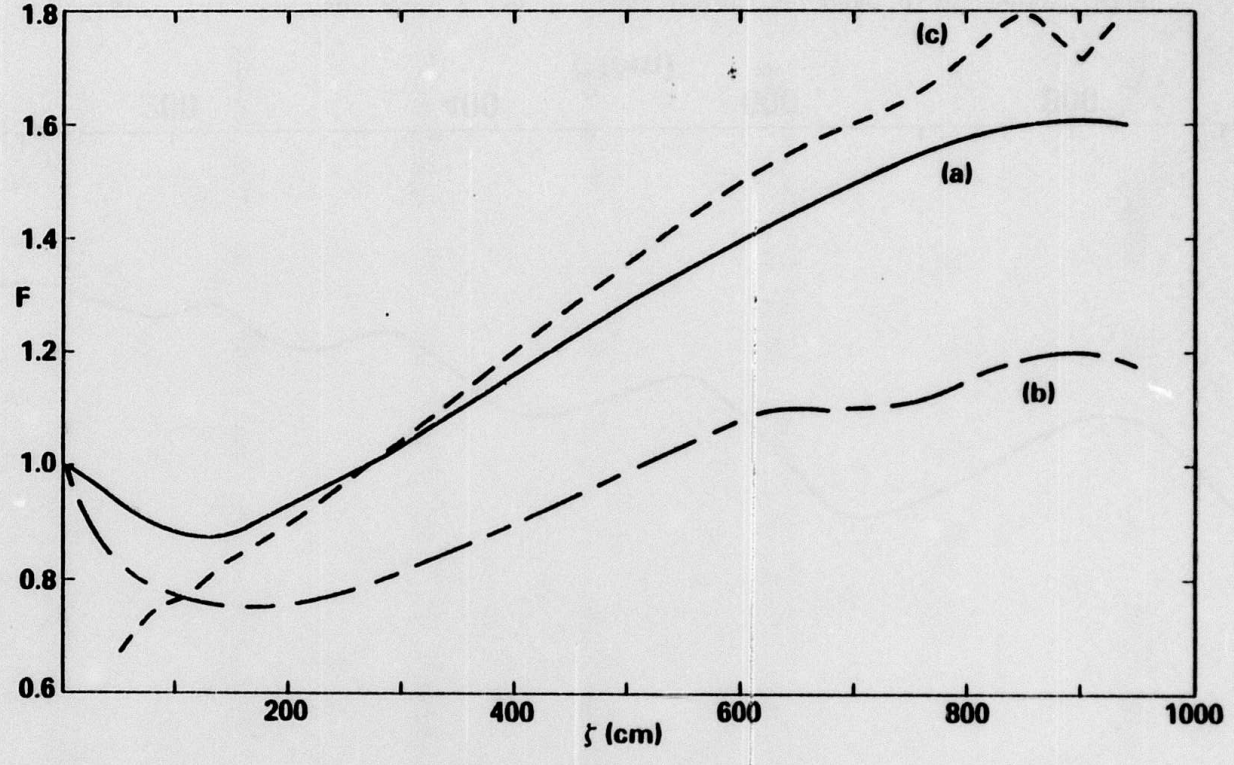

Figure 13: Current gain F as a function of ζ for the circularly polarized beam displacement described in Sec. 4.2. Beam radius a = 1 cm and pipe radius b_{pipe} = 7 cm for curve (a). For curve (b), a = 1 cm and b_{pipe} = 49 cm. For curve (c), a = 0.75 cm and b_{pipe} = 7 cm.

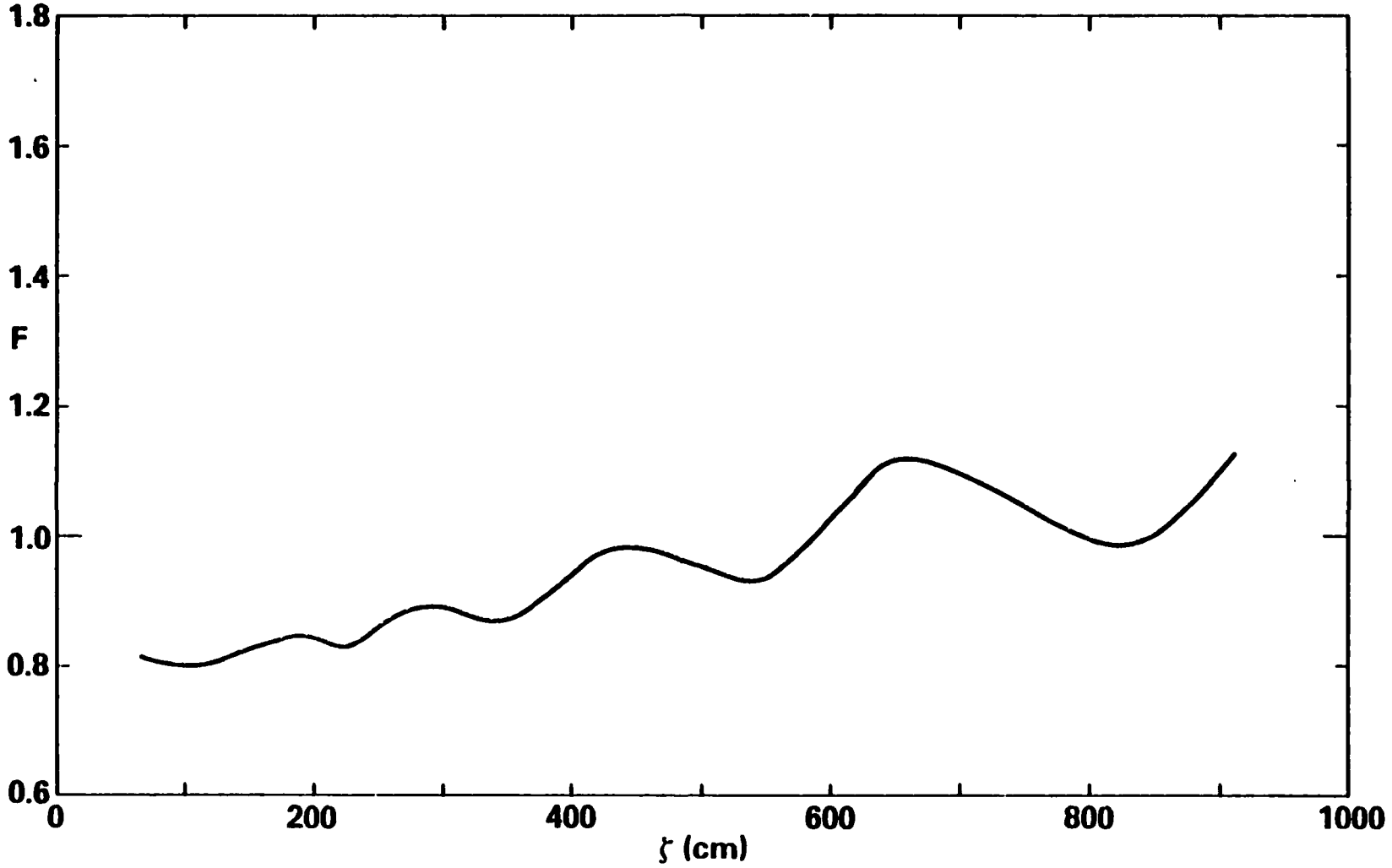

Figure 14: Current gain F for a plane polarized beam displacement with $a = 1$ cm and $b_{pipe} = 7$ cm.

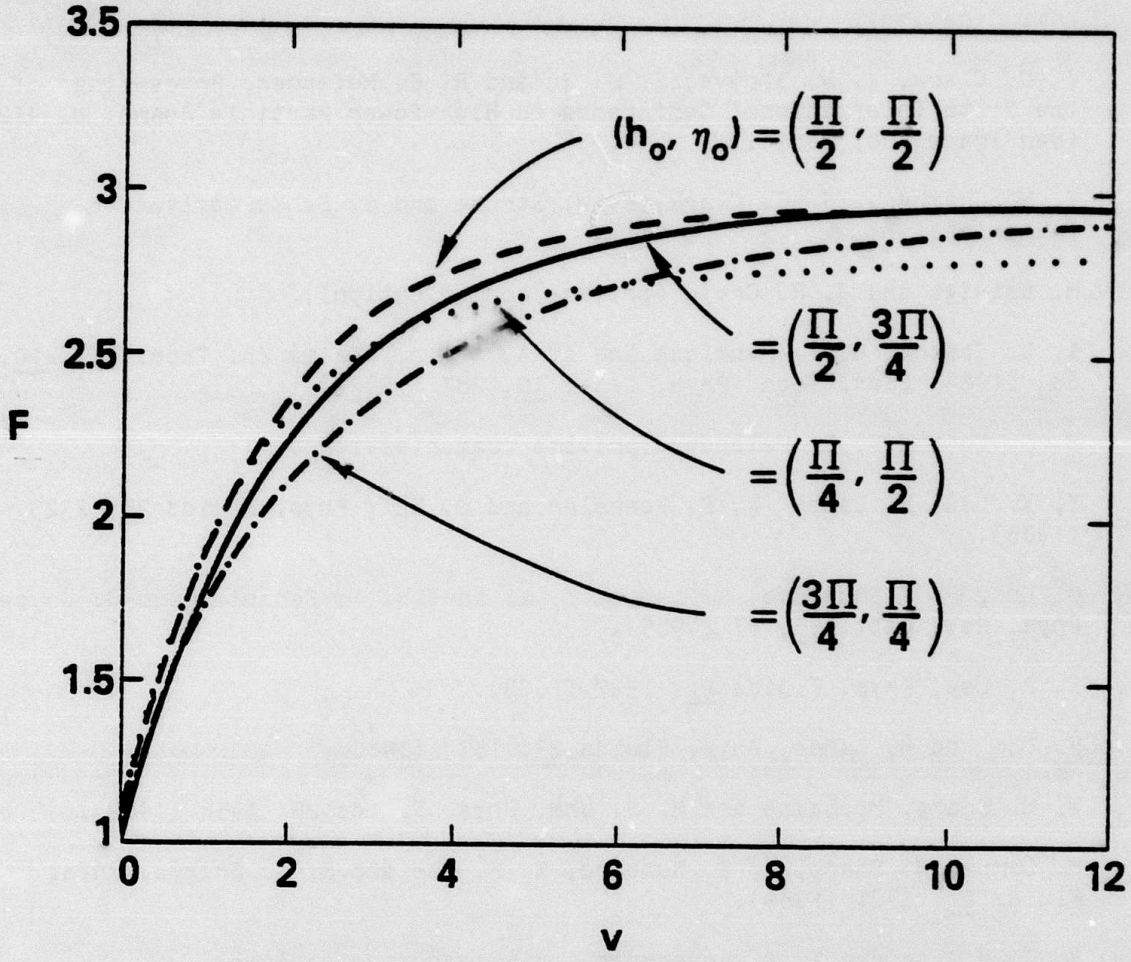

Figure 15: Current gain F as a function of v for various initial locations (h_o, η_o) of the current source.

References

1. F. W. Chambers, Phys. Fluids 22, 483 (1979).

2. R. J. Briggs, J. C. Clark, T. J. Fessenden, R. E. Hester and E. J. Lauer, Proceedings of the Second International Topical Conference on High Power Electron and Ion Beam Research and Technology, Vol. 1, p. 319 (Cornell University, Ithaca, New York, 1977).

3. J. C. Clark, E. J. Lauer, D. S. Prono and K. W. Struve (private communication).

4. J. C. Clark, K. W. Struve, S. S. Yu and R. E. Melendez, Proceedings of the Fifth International Conference on High-Power Particle Beams, p. 412 (San Francisco, 1983).

5. F. W. Chambers, J. C. Clark, K. W. Struve and S. S. Yu (private communication).

6. M. Raleigh and J. R. Greig (private communication).

7. A. L. Ipatov, G. P. Mkheidze and A. A. Savin, Pis'ma Zh. Tech. Fiz. 10, 681 (1984) [Sov. Tech. Phys. Lett. 10, 287 (1984)].

8. S. S. Yu and R. E. Melendez (private communication).

9. Y. Y. Lau, M. Lampe, R. F. Fernsler and B. Hui, Phys. Fluids 28, 2323 (1985).

10. B. Hui, R. F. Hubbard, M. Lampe, Y. Y. Lau, R. F. Fernsler and G. Joyce, Phys. Rev. Lett. 55, 87 (1985).

11. E. P. Lee, Phys. Fluids 21, 1327 (1978).

12. H. Uhm and M. Lampe, Phys. Fluids 23, 1574 (1980).

13. W. M. Sharp, M. Lampe and H. S. Uhm, Phys. Fluids 25, 1456 (1982).

14. M. Lampe, W. Sharp, R. F. Hubbard, E. P. Lee and R. J. Briggs, Phys. Fluids 27, 2921 (1984).

15. R. B. Miller and K. A. Brueckner (private communications).

16. H. S. Uhm and M. Lampe, Phys. Fluids 25, 1444 (1982).

17. M. Lampe and G. Joyce, Phys. Fluids 26, 3371 (1983).

18. G. Joyce and M. Lampe, Phys. Fluids 26, 3377 (1983).

19. E. P. Lee, F. W. Chambers, L. L. Lodestro and S. S. Yu, Proceedings of the Second International Topical Conference on High Power Electron and Ion Beam Research and Technology, Vol. 1, p. 381, (Cornell University, Ithaca, New York, 1977).

20. W. Fawley, R. L. Feinstein, K. Brueckner and J. S. Wagner (private communications).

21. R. F. Hubbard, J. M. Picone, G. Joyce and S. P. Slinker, unpublished (1985). See also R. F. Hubbard, G. Joyce, S. P. Slinker, M. Lampe and J. M. Picone, Bull. Am. Phys. Soc. 30, 1583 (1985).

22. E. P. Lee, unpublished (1976). See also Ref. 14.

23. J. R. Freeman and J. S. Wagner, Bull. Am. Phys. Soc. 29, 1290 (1984).

24. B. B. Godfrey (private communication).